

Independent estimates of net carbon exchange in croplands: UAV-LiDAR and machine learning vs. eddy covariance

Jaime C. Revenga¹, Katerina Trepekli¹, Rasmus Jensen¹, Pauline S. Rummel¹,
Thomas Friborg¹

¹Department of Geosciences and Natural Resources Management (Section of Geography), Copenhagen University,
Denmark

¹Øster Voldgade, 10, 1350 Copenhagen, Denmark

Key Points:

- The plant carbon budget in croplands estimated from UAV-LiDAR and machine learning regression is comparable with the carbon ecosystem uptake estimated via the eddy covariance technique.
- The relative match between the UAV-based method and the flux-based method along the two growing seasons (2.5% in 2020, and -9.0% in 2021) indicates that the UAV-based method is a valuable tool for plant carbon stock assessments and adaptive crop management in croplands.
- The proposed method has the potential to estimate cumulative CO₂ fluxes over areas not covered by direct eddy covariance flux measurements.

Corresponding author: Jaime C. Revenga, contact: jar@ign.ku.dk

19 **Abstract**

20 Understanding sequestration of organic carbon (C) in agroecosystems is of primary importance
21 for greenhouse gas (GHG) accounting in managed ecosystems, reducing the environmental footprint
22 of land use, and inform crediting programs. However, a broader application of precise C accounting
23 is currently constrained by a limited number of direct flux measurements. Aside well-studied
24 ecosystems via the eddy covariance technique (EC), many still bear significant uncertainty. In
25 this study, we propose and evaluate a method for estimating accumulated C stocks in agricultural
26 sites, by assessing the plant aboveground carbon (AGC) throughout the growing season using
27 unstaffed aerial vehicles and machine learning (ML) regression methods. Then, we benchmark
28 these estimates with CO_2 fluxes derived from the eddy covariance method from the ICOS DK-
29 Vng site in Denmark. We utilized a light detection and ranging (LiDAR) sensor onboard an
30 unstaffed aerial vehicle (UAV) to derive the structural characteristics of crops, and we conducted
31 in parallel destructive field-based measurements of AGC. Then, we designed a ML pipeline to
32 provide estimates of AGC as a supervised regression problem, using the LiDAR-derived point
33 cloud data to extract predictive features and the AGC labels as ground-truth target values. The
34 best performing ML model attained predictions of $R^2 = 0.71$ and $R^2 = 0.93$ at spatial resolutions
35 of 1 m^2 and 2 m^2 , respectively. The C content in the aboveground plant components was assessed
36 via laboratory analysis ($46.6 \pm 0.3\%$ of C-to-biomass in barley and $47.7 \pm 0.3\%$ in wheat), while
37 the belowground components (root allocation and rhizodeposition) were estimated based on a
38 phenology-dependent allometric ratio. The cumulative value of C uptake along the growing season
39 (i.e. NPP) was compared with the difference of C predictions between every two UAV-LiDAR
40 survey dates, finding an optimal disagreement between methods below $\pm 9\%$ in two different
41 cereal crops. The plant carbon budget in croplands, determined through UAV-LiDAR and machine
42 learning regression, aligns with the carbon ecosystem uptake estimated through the eddy covariance
43 technique, showcasing comparable results. Thereby, the proposed method also demonstrates the
44 potential to estimate cumulative CO_2 fluxes in areas lacking direct eddy covariance measurements.
45 Various experimental setups are evaluated as well as the sources of uncertainty resulting from the
46 sampling design.

47

48 **This PREPRINT manuscript is currently being considered for formal peer-reviewed**
49 **publication. Please note that, this is the submitted version of the study, and has yet**
50 **to be formally accepted. Subsequent versions of this manuscript may present slight**
51 **differences in content. If accepted, the final version of this manuscript will be**
52 **updated with the accepted manuscript. This preprint will also be linked to the**
53 **formal publication via its Digital Object Identifier (DOI). Please, feel free to contact**
54 **any of the authors; we welcome feedback.**

55

1 = Introduction =

The agricultural sector is the world's second-largest greenhouse gas (GHG) emitter, after the energy sector, accounting for a quarter of total global anthropogenic GHG emissions [1]. While agriculture is a driver of climate change, the observed climate alterations have in turn challenged the global crop productivity in the last decades [2, 3]. Without technological adaptations and dedicated mitigation measures [4], the environmental effects of agriculture could increase by 50–90% [5], and the global crop productivity might be reduced by 17% by 2050 [6]. To date, the adoption of climate-resilient and low-emission practices in agriculture has not yet reached the recommended levels [5]. Further, in most countries, the accounting of emissions for land-use and agriculture relies on simple upscaling of standardized values, with little to no data-driven validation procedures. This is hindering accurate GHG accounting as well as attaining environmental and economically efficient solutions.

Monitoring carbon (C) sequestration and CO₂ emissions from croplands is a prerequisite for the effective design of sustainable agricultural management schemes. In a changing global climate, different regions undergo contrasting extreme weather events such as drought, heavy precipitation, shifts in timing and length of growing seasons, or heat stress [7]. This highlights the necessity to quantify the C sequestration capacity with techniques tailored to specific ecosystems' conditions. In this context, precision agriculture is regarded as a promising set of methods for sustainable intensification, in order to close yield gaps while reducing GHG emissions [8, 9, 10]. Precision agriculture targets the reduction of agriculture's impact on the environment, while optimizing crop yield [11] with data-driven methods.

The standard framework to account for the transit of atmospheric CO₂ is the net ecosystem exchange (NEE) [12], i.e. the net CO₂ flux at the atmosphere-biosphere interface (Figure 1). NEE is calculated as the difference between CO₂ uptake via photoassimilation (i.e. gross primary productivity, GPP) and the release of CO₂ via ecosystem respiratory losses (R_{eco}) [12]. Another commonly used metric in ecosystem budgeting is net primary productivity (NPP), which, unlike NEE, does not explicitly include soil-derived fluxes (e.g. heterotrophic respiration). Therefore, it reflects the photosynthetic productivity of vegetation alone [13]. Thus, NPP is the most direct surrogate measure for plant growth, which is derived from the flux-based eddy covariance framework and the soil respiration component.

At the ecosystem scale, C budgets are usually reported as a range of confidence for C estimates, rather than specific values [14]. This is due to the fact that ecosystem-level estimates are bound to co-occurring complex phenomena, so that it is necessary to count on certain assumptions (e.g. negligible levels of lateral carbon fluxes and heterotrophic respiration, atmospheric turbulence conditions reached, etc.) which affect the estimates' accuracy. In fact, studies focused on different regions have reported large inter-annual variability in C fluxes from croplands, which act either as net sinks [15], net sources [16, 17], or as relatively C neutral [18]. In order to assess the consistency of the net ecosystem carbon balance (NECB), established approaches involve comparing a measured quantity (e.g. NEE) obtained at the same temporal and spatial scale using independent methods [19, 20, 21, 22, 23]. This is usually done via either: (i) micrometeorological methods to assess the ecosystem-atmosphere fluxes; (ii) inventories of stock changes in the biomass and soil; or (iii) bottom-up modelling of ecophysiological processes from flux chamber measurements. Such consistency assessments require that all NECB components are estimated during the same time intervals [24].

100 In practice, the components of the NECB, besides lateral fluxes, are directly measured by the
101 eddy covariance (EC) technique or derived from such measurements [25], which is to date the state-
102 of-the-art to obtain ecosystem-level flux estimates. However, there are limitations associated with
103 the EC method, namely, (i) being bound to local measurements with costly instrumentation fixed
104 to the ground, and (ii) requiring specific atmospheric conditions. This method also involves the
105 assumption of representativeness, meaning that areas monitored by the EC method are expected
106 to be representative of broadly defined ecosystem types. However, observational gaps exist [26]
107 and single ecosystem types may not be sufficiently account for the effects of local environmental
108 conditions and management practices. Hence, it is needed to advance methods to improve the
109 flexibility of C estimates, where approaches based on mobile platforms have proven useful [26, 27,
110 28, 29].

111 The primary motivation for advancing methods based on Unmanned Aerial Vehicles (UAVs) is
112 to leverage the flexibility and scalability that mobile platforms offer. This allows for independence
113 from restrictions associated with the use of fixed instrumentation. In the last decade, UAV methods
114 developed for crop phenotyping and flux research have provided significant advances [26, 27, 28,
115 29]. The integration of UAV-based data and ecosystem modelling has seen recent advances: Wang
116 et al. (2020) [26] introduced a method for estimating interpolated land surface fluxes derived
117 from a combination of UAV-based imagery and a dynamic modelling, finding that the UAV-based
118 method proved useful in calibrating soil and vegetation parameters, achieving C flux estimates
119 within 13-15% of agreement with the EC measurements. Moreover, UAV-based remote sensing
120 is increasingly used to assess aboveground biomass (AGB) and carbon stocks, thanks to mobile
121 sensors' capacity to capture land surface variables with high spatial resolution and flexible revisit
122 times [30]. To date, the majority of studies use UAV-photogrammetry (e.g. structure-from-motion
123 techniques) to calculate AGB as a function of plant height metrics (e.g. maize [31, 32, 33, 34],
124 rice [35], spring barley [36, 37], cotton [38], or winter wheat [39, 40]). Yet another line of research
125 aims to assess AGB as a function of vegetation indices using spectrally resolved sensors (e.g. spring
126 wheat [41], winter wheat [42, 43, 44], corn and soybean [45], and rice [46]).

127 More recently, the emergence of mobile light detection and ranging sensors (LiDAR) has
128 not only upgraded the spatial resolution of datasets, but also included the vertical component,
129 creating truly volumetric representations (i.e. point clouds). This has allowed to enhance crop
130 phenotyping [47] and map AGB in croplands at a sub-meter resolution [30] by leveraging the
131 structural information of vegetation from 3D point clouds. UAV-LiDAR methods have provided a
132 workaround to previous obstacles in UAV-based crop phenotyping, namely the spectral saturation
133 in image-based vegetation indexes, especially during maturity of crops. Following this research line,
134 we build on recent studies on AGB mapping in cereal croplands using UAV-LiDAR technology [30]
135 and previous micrometeorological work on ecosystem flux exchange [18] to investigate the level of
136 agreement between independent estimates of ecosystem C exchange.

137 Here, we explore the level of agreement between two independent methods to estimate cumu-
138 lative C exchange in cereal croplands: (i) UAV-LiDAR surveying combined with ML regressions,
139 and (ii) flux-based EC measurements. We compare simultaneous and independent estimates of
140 photoassimilated C exchange, in a crop field in Mid-Jutland (DK), over two consecutive years.
141 Specifically, we propose and evaluate a method to estimate *in situ* plant C using UAV-LiDAR and
142 machine learning (ML) regressions, and compare the results obtained with the respective NPP
143 during identical time intervals. The motivation of this study is to leverage the capabilities of UAV-
144 LiDAR sensors and ML regressions in order to provide estimates of cumulative plant C stocks in

145 croplands, thereby contributing to advancing current techniques in ecosystem CO₂ budgeting from
 146 mobile platforms.

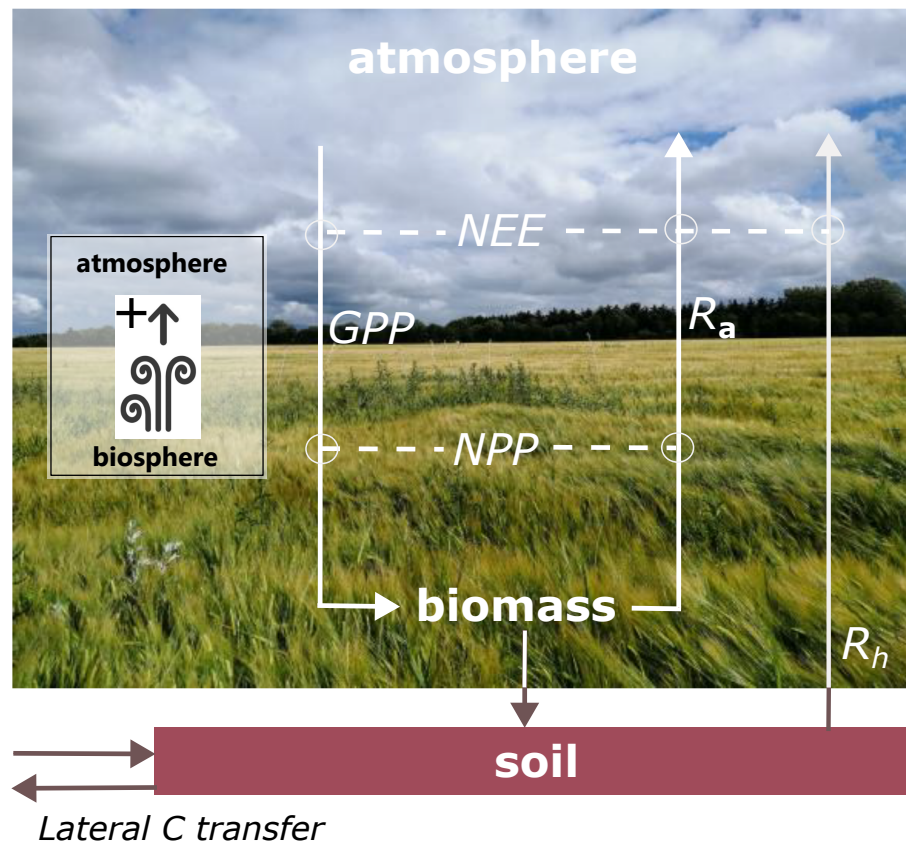


Figure 1. Components of the net ecosystem carbon balance (NECB). The inset on the left indicates the sign convention for fluxes calculation. NEE: net ecosystem exchange. GPP: gross primary productivity. NPP: net primary productivity. NEE: net ecosystem exchange. R_a : autotrophic respiration. R_h : heterotrophic soil respiration. Lateral carbon transfer refers to human intervention (e.g. harvest, fertilization).

147 2 = Materials and Methods =

148 2.1 Study Area

149 The study area (Figures 1 and 2) is a conventionally managed cropland site located around
 150 an Integrated Carbon Observation System (ICOS) [48] class-1 ecosystem station at Voulund, (DK-
 151 Vng) in Mid-Jutland, Denmark (56.037476N, 9.160709E). Located on the eastern part of the Skjern
 152 River catchment, covering an area of ca. 13 ha. The field is a flat plain at an altitude of 64-68 m
 153 above mean sea level, with smooth undulations and a slight slope to the northwest. The ploughing
 154 layer (30 cm deep) sits on a sandy soil (ca. 99% sand) with pebble inclusions of ca. 3-5 diameter.
 155 The water-table depth lies at 5.5 ± 1 m below ground. The region presents a humid temperate
 156 climate characterized by a mean annual precipitation of 961.0 mm, mean annual temperature of
 157 8.1 °C, and usually overcast or scattered cloud cover (mean annual incoming short-wave radiation

158 of 108 W/m^2). For an insightful description of both functional and topographic characteristics of
 159 the Voulund agricultural site, the reader is referred to Jensen et al. (2016) [18].

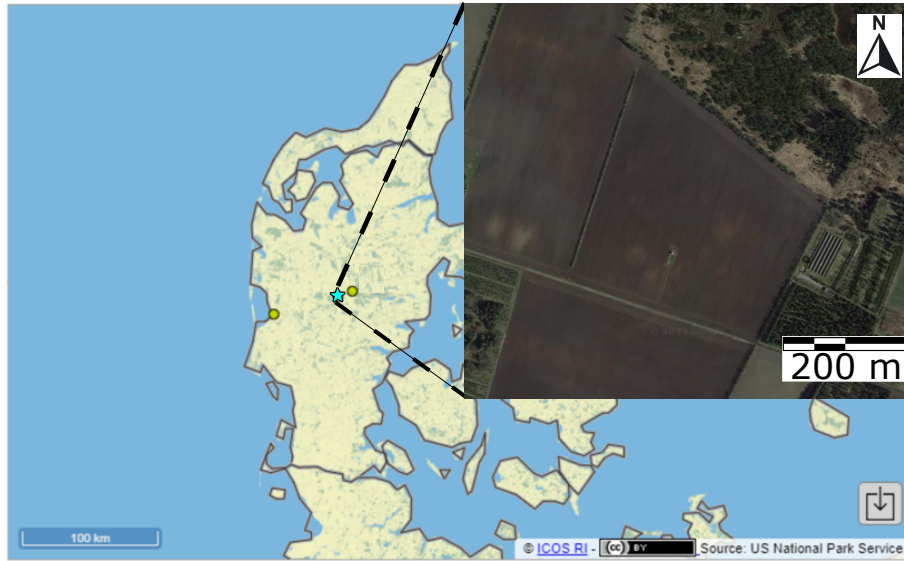


Figure 2. Location of the study site (★) in Mid-Jutland (DK). The inset shows a top-down view of the field site and the surrounding area. Source: www.icos-cp.eu and Google Earth Engine.

160 The crops investigated were spring barley (*Hordeum vulgare L.*) and winter wheat (*Triticum*
 161 *aestivum L.*) during 2020 and 2021, respectively. The growing period of the barley crops lasted
 162 from the end of 04/2020 (seedling emergence) to the end of 08/2020 (harvest), following a similar
 163 cycle in the 2021 season. In 2021, the growing period of winter wheat extended from 01/2021
 164 (seedling emergence) until the end of 08/2021 (harvest). The conventional agricultural practice
 165 at the site included the application of fertilizers in the form of pig slurry, according to ministerial
 166 regulations [49], pesticides along the growing season, as well as sufficient irrigation to prevent water
 167 stress [18]. Applied fertilizer rates were bound to a maximum of 159 (N) and 21 (P) kg/ha, and
 168 202 (N) and 19 (P) kg/ha, for spring barley and winter wheat respectively.

169 2.2 UAV-LiDAR Survey and Point Cloud Data

170 We used a UAV-borne LiDAR system mounted to a DJI Matrice 600 Pro payload at a 90° pitch
 171 angle, and same heading and roll as the UAV platform. The system included a discrete infrared Li-
 172 DAR scanner (M8 sensor, Quanenergy Systems, Inc. Sunnyvale, CA, USA) and the corresponding
 173 industry standard inertial and navigation systems. In addition, we used a ground based differ-
 174 ential Global Positioning System (dGPS, Trimble R8) during the UAV-LiDAR survey, set up in
 175 post-positioning kinematic (PPK) mode, which logged real-time satellite coverage (cf. Ravenga
 176 et al. 2022 [30] for details on the airborne and ground system). The coupling of the satellite
 177 coverage data with the UAV-based laser and navigation data produced allowed the generation of
 178 georeferenced point cloud data (PCD) scenes, following Davidson et al. (2019) [50]. We visualized
 179 the PCD scenes of barley and wheat crops at maturity stage in Figure 3 (a and b, respectively).

180 UAV-LiDAR data were acquired according to the planned UAV-LiDAR survey at a height
 181 of 40 m above ground level. Following a regular auto-pilot flight grid, we ensured a 20% overlap

182 between individual LiDAR scans of ca. 50 m width and 250 pp/m² (cf. Revenga et al. 2022 [30]
 183 for additional details on applied flight parameters). The surveys were conducted during May-July
 184 2020, and during April-July 2021, coinciding with the two growing seasons.

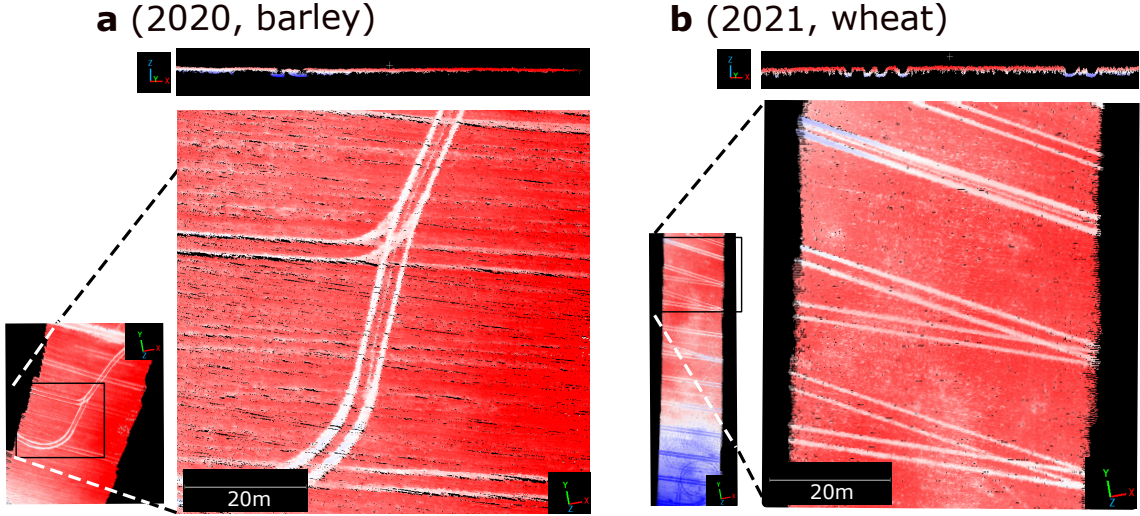


Figure 3. Point cloud data (PCD) scenes. The crops are portrayed at maturity stage. **a:** barley field, during 2020. **b:** wheat field, during 2021. The PCD scenes are colored by elevation. In both **a** and **b**, the upper panels show the cross section view of the PCD, with a buffer depth of 1m. Axes x , y , and z , indicate easting, northing, and elevation, respectively. A higher PCD porosity in **b**, than in **a** corresponds to a more sparse crop structure.

185 2.3 Field Based Destructive Measurements of Aboveground Carbon

186 Aboveground carbon (AGC) was the reference plant C component for ground-truth labelling,
 187 as a variable directly measured *in situ*. In contrast, the other plant C components considered
 188 (i.e. $root_C$ and rhizodeposits) were derived from AGC, phenology and reference literature. The
 189 estimates of $root_C$ are explained in Section 2.5, together with estimates of rhizodeposits.

190 In order to acquire reference values of crop AGC (i.e. ground-truth labels) to provide super-
 191 vision to the ML regression models, AGB samples were systematically collected from the field at
 192 random locations during the growing season, according to ICOS protocols for vegetation measure-
 193 ments [51]. The locations selected during sampling are visualized in Figure 4 (b).

194 During 2020 the AGB sampling procedure followed the standard ICOS protocol. In contrast,
 195 during 2021 this AGB sampling procedure was modified, in order to maximize data sample size
 196 with a limited fieldwork capacity. In such way, in 2021, at each location, three adjacent individual
 197 samples were collected (Figure 4, c). The AGB sampling scheme designed for 2021 allowed to
 198 produce an additional dataset composed of *augmented* samples. The augmentation procedure
 199 consisted of adding adjacent AGB samples, and their corresponding UAV-LiDAR data samples,
 200 so that both the AGB label and the corresponding LiDAR metrics could be recalculated from the
 201 resulting combined sample. The augmentation allowed to produce one larger dataset (specifically,
 202 with a sample size 4/3 times the original datasets' size) at a spatial resolution of 0.35-0.52 m² (cf.
 203 Revenga et al. 2022 [30] for a detailed explanation of the augmentation procedure). In total, three

204 separate datasets of AGB were produced: two were originally collected, plus a third one consisting
 205 of augmented samples.

206 The C contained within the aboveground crop biomass was assessed by the ICOS Ecosystem
 207 Thematic Center (ETC) [52], via conventional laboratory analysis from leaf tissue. The AGB
 208 samples were oven-dried for 72h at 65°, to assess the dry biomass weight. This evaluation involved
 209 determining the C-to-AGB ratio at 16 locations, using 45g of tissue from the uppermost and middle-
 210 height leaves at each location, during the peak of the growing season. For simplicity, we assumed
 211 this ratio constant across the aboveground plant components. Using the AGB prediction results,
 212 and the C-to-biomass ratio measured, we calculated the plant AGC. Following, we converted the
 213 point-based AGC estimates to surface-based values, so that the resulting reference AGC values
 214 were resampled to 1 m² resolution. In such way, we obtained a distribution of surface-based
 215 ground-truth estimates of AGC density. Table 1 provides a comprehensive overview of the sample
 216 count and spatial dimensions AGC reference labels in this study. The spatial distribution and size
 217 of the AGC datasets are visualized in Figure 4.

Table 1. Description of aboveground carbon (AGC) datasets. The subindex *aug.*, refers to the *augmented* dataset.

Growing season	dataset name	Number of samples	Sample dimensions (m)
2020	<i>barley</i> ₂₀	104	1 x 0.35
2021	<i>wheat</i> ₂₁	455	0.5 x 0.35
	<i>wheat</i> _{21,aug.}	609	(1-1.5) x 0.35

218 2.4 CO₂ Flux: Measurements and Calculation

219 The study site is equipped with state-of-the-art instrumentation complying with ICOS pro-
 220 tocols for a class-1 ecosystem station [48]. The equipment used for ecosystem flux measurements
 221 encompasses: an EC system constituted of Gill HS-50 sonic anemometers (Gill Instruments Ltd,
 222 Lymington, UK) and LI-7200RS enclosed infrared CO₂/H₂O gas analyzers (LI-COR, Lincoln, NE,
 223 USA) sampling at a frequency of 20Hz.

224 Additionally, the station is further equipped for air- and soil-meteorological monitoring, mea-
 225 suring the following variables: air temperature, relative humidity, air pressure, global radiation,
 226 photosynthesis active photon flux density, soil temperature, and soil water content [18].

227 *Raw data processing*

228 The raw data processing, quality control, and subsequent gap-filling procedures followed closely
 229 the standards applied by ICOS ETC [48, 53]. The EC data produced at DK-Vng became part of
 230 the ICOS ETC database only in 2021. For consistency, in order to apply the exact same treatment
 231 to the two datasets (i.e. 2020 and 2021), we processed the raw data in-house according to the
 232 ICOS ETC standards.

233 Raw 20 Hz wind, CO₂, water vapor, and sonic temperature data were processed utilizing
 234 the EddyPro v. 7.0.9 software (LI-COR, Lincoln, NE). Half-hourly turbulent scalar fluxes were
 235 calculated as the covariance between vertical wind speed and scalar variables (i.e. CO₂, H₂O, T).

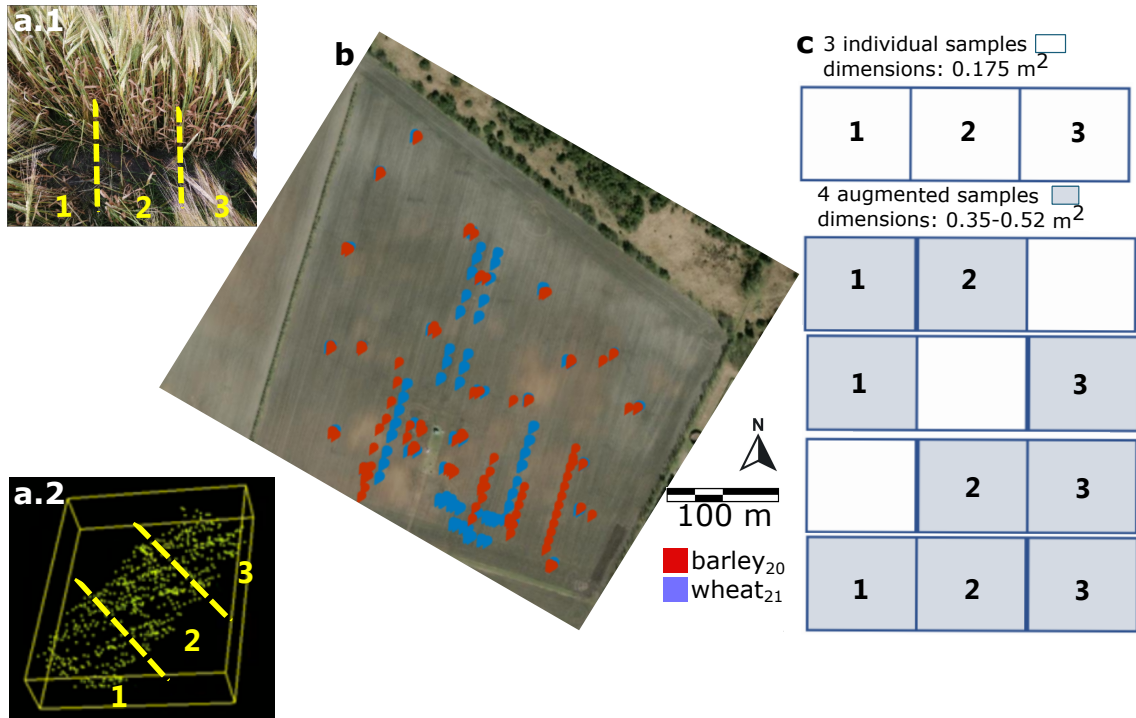


Figure 4. **a.1:** Three adjacent aboveground biomass samples (AGB) and the corresponding three LiDAR samples (**a.2**, dimensions of each sample: $0.5 \times 0.35 \text{ m}$). **b:** The spatial distribution of the AGB sampling locations. Each color indicates one of the original datasets: **red:** barley samples collected in 2020 (i.e. *barley*₂₀); **blue:** wheat samples collected in 2021 (i.e. *wheat*₂₁). **c:** dimensions of three original AGB samples (above), and data augmentation scheme by permutation (below); i.e. adding either two or three samples).

236 The processing included statistical tests for raw data screening [54], double coordinate rotation,
 237 block averaging, time-lag optimization to maximize covariance, compensation for the effect of
 238 density fluctuations on fluxes [55, 56], and low- and high-frequency spectral correction [57]. Half-
 239 hourly turbulent scalar fluxes were calculated as the covariance between vertical wind speed and
 240 scalar variables (i.e. CO_2 , H_2O , T).

241 *Post-processing: Spike Removal, Quality Control, and Gap Filling*

242 During raw data processing and post-processing, low quality data were rejected, following a
 243 standard data screening procedure. This operation consists of two sub-tasks: (i) an absolute limit
 244 test, that sets boundaries for a physically plausible range of values, and (ii) individual outliers
 245 were detected following the method proposed by Papale et al. (2006) [58]. Additionally, data were
 246 removed when the wind came from the direction covering the instrumental plot (Figure 5, b), so
 247 we prevented the instrumentation from influencing the measurements.

248 The data rejected left therefore gaps in the datasets of both years. During 2020's growing
 249 season, this resulted in a 56.8% of data rejected after all three filtering tests were applied. While the
 250 gaps occurred mainly at the beginning and end of the 2020 year (Autumn and Winter), the growing
 251 season was better populated with valid NEE data values. The data were gap-filled according the

method proposed by Reichstein et al. (2005) [59], and the u^* -filtering procedure was based on season. The processing of the 2021 flux dataset followed the same procedure as for the 2020 season. The processed data showed a missing ratio of 32.9% after the quality control test and de-spiking, showing fewer gaps than the previous year and also a better flux data recording during the growing season. To acquire a continuous dataset and allow for the estimation of cumulative carbon budgets, data gaps were filled following the method of Reichstein et al. (2005) [59], using the [REddyProcWeb](#) tool. The method combines lookup tables of average fluxes under comparable meteorological conditions in a certain time window. If meteorological measurements are missing, fluxes are estimated as the mean flux at the same time of the day in each time window (i.e. mean diurnal course). A detailed description of the EC system, raw data processing and post-processing routines at this same EC station can be found in Jensen et al. (2017) [18].

Estimation of Flux Climatology Footprint

We calculated the flux climatology footprint using the model developed by Kljun et al. (2002) [60], and extracted the polygon covering the 70% influence around the station (Figure 5, a). The reason to select specifically the 70% area of influence around the EC station followed the criterion of maximizing the surface covered before reaching disruptions in the vegetation cover (e.g. hedgerow, gravel road), so it is ensured that the measured signal comes only from the vegetation. This allowed to make the surveyed area representative of different crop canopy structures, and to benefit from the cancelling of statistical errors, through spatial averaging effects [30, 61], thereby reaching optimal predictions of AGC at the footprint scale.

Furthermore, in order to remove the influence of the instrumental plot surrounding the EC tower on the measurements, this area was masked out. For the 2020 dataset, the wind directions that covered the instrumental plot (18–198°) were excluded of further processing. The wind directions excluded in 2021 differed slightly from the previous year (the directions masked covered the section 18–116°), as the size of the experimental plot had to be reduced in 2021 (Figure 5, b.1 and b.2).

Ecosystem Flux Balance

After data processing, the flux data provide an estimate of the net ecosystem exchange (NEE) (Figure 11, Annex I), allowing to estimate other NECB components. The estimation of net primary productivity (NPP) involved calculating the difference between NEE and ecosystem respiration. Therefore, we considered the flux balance

$$NPP = (-NEE) + R_h \approx (-NEE) + R_{soil} \quad (1)$$

where R_h accounts for the heterotrophic respiration, while the autotrophic plant respiration is contained within NPP. As per the micrometeorological sign convention, the negative sign indicates flux direction towards the ecosystem; the positive sign indicates a flux release towards the open atmosphere. In conventional croplands, where the influence of higher-order heterotrophs (e.g. mammals, birds) can be considered negligible, the microbial soil respiration (R_{soil}) constitutes R_h [62]. Here, we modeled R_{soil} as a function of soil temperature during winter, as prior to the onset of the photosynthetic season the site consisted of plain bare ground, hence allowing to model heterotrophic respiration. Following Lloyd and Taylor (1994) [63], a second-order polynomial

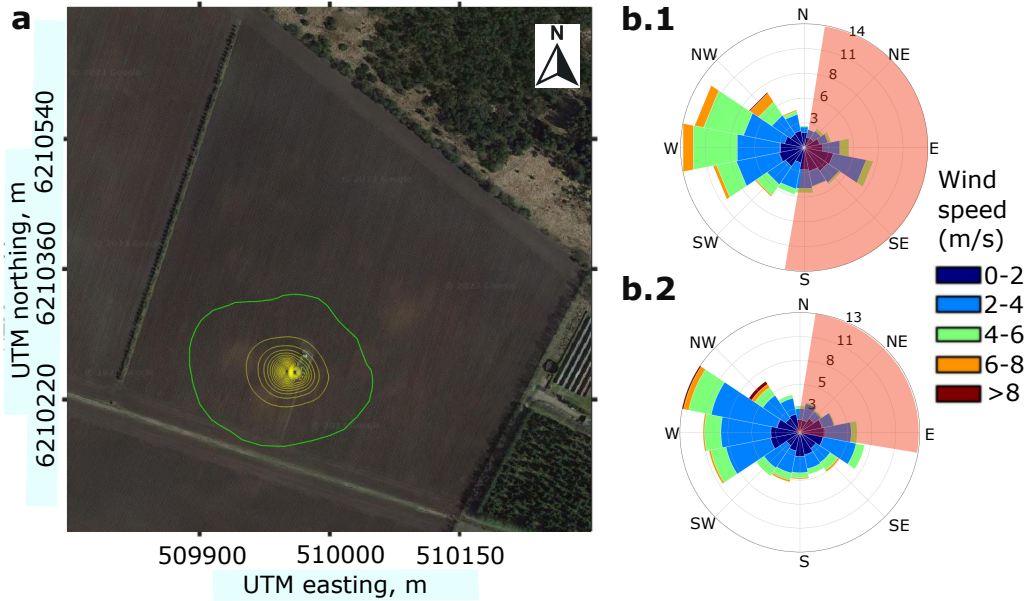


Figure 5. **a:** Flux footprint climatology map from the study site; the yellow contours indicate areas of 10% increase of influence (source of background image: Google Earth 2023). **b.1, b.2:** wind frequencies at the study site during April–August of 2020 and 2021, respectively. The radius indicates total frequency of a given wind direction; the color indicates wind speed (ms^{-1}). The shaded red areas cover the wind directions influenced by the instrumental plot—which were filtered out for flux analysis.

291 was fitted to the measurements of NEE prior to the start of the growing season (i.e. constituted of
 292 the R_h component only), as function of soil temperature 5 cm below surface. We filtered out R_{soil}
 293 values corresponding to frozen conditions (i.e. < 0.5 °C) for the model fit. Then, we extrapolated
 294 the modeled R_{soil} to the entire growing season.

295 2.5 Root and Soil Carbon Estimates

296 Unlike AGC, we did not assess $root_C$ based on direct measurements. Instead, $root_C$ was esti-
 297 mated based on the sampled AGC, reference literature [64, 65, 66] and a linear dynamic allometric
 298 model based on the phenological growth stage [67].

299 The total plant C estimates (i.e. AGC plus $root_C$) were obtained by calculating at each point
 300 the total plant C derived from the AGC prediction. In order to obtain this estimate, we considered
 301 the allocation of $root_C$ as a dynamic quantity, dependant on the phenological stage, using Eq. 2.
 302 We fixed $root_C$ at anthesis as $10 \pm 1\%$ of total plant C at maturity of crops, according to reference
 303 literature [64]. Likewise, the amount of the photosynthesized C (i.e. GPP) [62] was used to
 304 model the rate at which the assimilated C is translocated to the roots, according to reference
 305 literature [65].

306 Therefore, $root_C$ was calculated as a function of (i) AGC, (ii) the rate at which GPP is
 307 translocated to the roots (GPP_{roots}), and (iii) the phenological stage (i.e. x_{ph}) [67]:

$$root_C(x_{ph}) = \begin{cases} x_{ph} \cdot GPP_{roots}, & \text{if } x_{ph} < x_{anthesis} \\ (0.1 \pm 0.01) \cdot AGC_{mat}, & \text{if } x_{ph} = x_{anthesis} \\ root_{C,post}(x_{ph}), & \text{if } x_{ph} \geq x_{anthesis} \end{cases} \quad (2)$$

308 where AGC_{mat} indicates aboveground carbon at maturity stage; the function $root_{C,post}(x_{ph})$
 309 defines the C stock in roots at any phenological stage posterior to anthesis. It was defined by a linear
 310 fit to $root_C$ at anthesis and values of GPP_{roots} reported in literature at the phenological stages
 311 posterior to anthesis, for wheat and barley in sandy soils, respectively [65]. Similarly, GPP_{roots}
 312 was obtained as the slope of a linear fit between the onset of the season and $root_C$ at anthesis.
 313 This estimate resulted on an average translocation of GPP to roots along the whole season of 13%
 314 and 14% for barley and wheat, respectively.

315 Lastly, we assessed the quantity of photoassimilated carbon translocated to the soil as rhizode-
 316 position (i.e. $rhizo_C$) relying on information from reference literature. In conventionally managed
 317 crop fields, $rhizo_C$ in sandy soils has been previously measured using stable C isotope labeling and
 318 reported as a relative fraction of GPP [66, 68]. Therefore, $rhizo_C$ was calculated as a linear fit to
 319 the values reported in literature for barley and wheat, specific to sandy soils. This resulted on an
 320 average translocation of GPP to rhizodeposits of 2.7% and 1% for barley and wheat, respectively.

321 2.6 Machine Learning-based Carbon Estimates

322 2.6.1 Training and Validation of Predictions

323 Three different ML regression models were initially selected for the task of AGC prediction.
 324 They were calibrated on a training dataset, and their performances were evaluated on a separate
 325 validation dataset; then, the best performing one was chosen for testing. This procedure helped
 326 avoid overfitting the model to the data, preventing an optimistically-biased accuracy assessment.

327 Therefore, we selected three fundamentally different ML methods; one representative of regu-
 328 larized linear models (i.e. Huber regressor) [69, 70], one tree-based ensemble method (i.e. Extreme
 329 Randomized Trees, ERT) [71], and one exemplar from the boosting methods (i.e. Extreme Gradi-
 330 ent Boosting, XGBoost) [72].

331 The model performance on the validation set was assessed via the average performance (in-
 332 dicated by the overbar) of the following metrics over 10 randomized executions: coefficient of
 333 determination ($\overline{R^2}$), mean squared error (\overline{MSE}) and mean absolute error (\overline{MAE}). ERT obtained
 334 the best results across all four scores and therefore was selected as the model of choice. For more
 335 details on the model selection, validation and test procedure cf. Revenga et al. (2022) [30].

336 2.6.2 Description of the Model Selected

337 Extremely Randomized Trees (ERT) is an ensemble learning technique that aggregates the
 338 results of multiple individually created decision trees to output, e.g. regression results. Originally
 339 derived from the Random Forest model [73], in an ERT model every individual predictor—i.e.
 340 a binary decision tree—is constructed from a random selection of features without replacement
 341 from the whole training set. A single tree decides at each node, which split—of a random subset
 342 of feature splits—reduces the reconstruction error (e.g. MAE or MSE) the most. The random

sampling of predictive features, plus the randomization step at each split node, leads to more diverse and thus less correlated decision trees, thereby leading to improved generalization results, and lower training times. Each tree is considered to be a “weak” regressor performance-wise but the combination creates an ensemble that outperforms the individual regressors. As final prediction, the average predictions of the individual decision trees in the forest is used, providing as output an estimate of above ground carbon (i.e. \widehat{AGC}).

2.7 Comparison of Independent Carbon Estimates

In order to quantify the degree of convergence between the UAV-LiDAR-based method and the flux-based method, we conducted a date-by-date cross comparison. This analysis allowed us to assess the degree of agreement between the two techniques at each single survey date, as well as to spot sources of inconsistency. To that end, we used the following metric, referred to as delta-ratio (Δ_C). It is defined as the ratio between the increment of plant C (measured via UAV-LiDAR) and the increment in NPP (obtained via the EC method) between two separate surveying dates:

$$\Delta_C = \frac{\Delta(NPP_{i,j}) - \Delta(PlantC_{i,j})}{\Delta(NPP_{i,j})} \cdot 100 \quad (3)$$

where the subindexes i, j refer to two different surveying dates. The results of this analysis allowed us to inspect sources of mismatch between methods as well as to discern which experimental setup resulted optimal.

3 = Results =

Temporal Development of Biomass and Carbon

The AGB sampling along 2020 and 2021 resulted in two distinct curves of AGB build-up (Figure 6 a and b). It can be observed that, while in 2020 a saturation plateau of plant AGB was reached (1 July 2020), in 2021, the saturation point was not reached by the time of the last biomass survey date (14 July 2021). The shaded ribbon around the time series of AGB in both years, covering the 68% confidence interval, is remarkably wider at the end of 2021’s season than at the end of 2020’s season. This is consistent with a more open canopy structure (Figure 3) corresponding to a more heterogeneous and sparser AGB density, as well as lower total plant C accumulation.

In 2020, the AGB collection campaign started at a level of 100 gm^{-2} . In Figure 6 (a) it can be observed a steady increase of AGB until 1 July, where there is a turning point, and a saturation plateau afterwards. From then onward, AGB stabilizes, and by the harvesting date (end of July) the AGB are just slightly above the one measured on 1 July. In contrast, during the 2021 season, we started the AGB sampling campaign at a point slightly above 0 gm^{-2} , in order to extend the span of AGB measurements. It can be noted a slow start of AGB accumulation. By approximately the same date (27 May), the AGB in 2021 growing season lags 150 gm^{-2} behind the previous year. Instead of saturating by 1 July, AGB kept growing until the last sampling date. This finding was expected, considering that the crops in 2021 exhibited a lagged development of approximately 15 days compared to the previous year. This is mainly explained by the extensive periods with freezing temperatures that the crops of 2021 endured at the onset of the season (see Annex I). This lag in AGB accumulation in 2021 with respect to 2020 can be compared with the corresponding

381 time-lag observed in the ecosystem fluxes of both years (Figures 11 and 12, in Annex) showing
 382 that e.g. in 2021, by the start of June, GPP barely offsets the ecosystem respiratory losses (R_{eco}).

383 The seasonal development of AGC follows the same dynamics as AGB, given that we assumed
 384 both variables to be linearly related. As a result of the lab analysis, we modelled the C content
 385 to be constant across all the aboveground plant tissue: $46.6 \pm 0.3\%$ in barley, and $47.7 \pm 0.3\%$
 386 in wheat. Consequently, the difference in total plant-mediated C by the end of both seasons was
 387 estimated as 88 g/m^2 higher in 2021 than in 2020 (Table 2).

388 As regards the temporal development of belowground C transport, wheat translocates a
 389 slightly greater amount of photoassimilated C to roots and soil compared to barley, in rela-
 390 tive terms [65]. This different strategy becomes increasingly evident as the growing season pro-
 391 gresses (Figure 8).

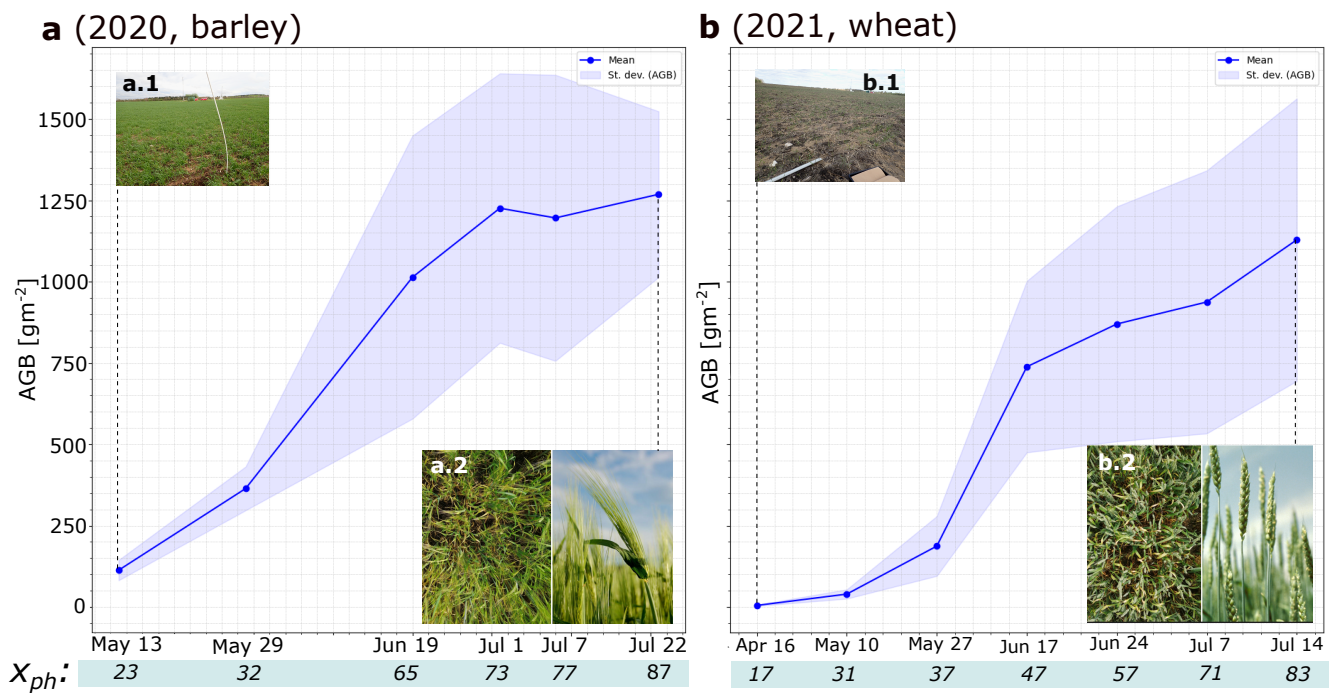


Figure 6. Crop aboveground biomass (AGB) development during 2020 (a, barley) and during 2021 (b, wheat) growing seasons, respectively. Dates on x-axis indicate the dates of AGB sampling; y-axis indicates dry AGB matter. The blue solid line indicates the mean per sampling campaign and the shaded area covers \pm the standard deviation. **a.1, a.2:** spring barley crop structure at the start of the sampling campaign and at maturity stage, respectively. x_{ph} : phenological growth stage (Zadoks decimal code) [67]. **b.1, b.2:** winter wheat crop structure at the start of the sampling campaign and at maturity stage, respectively. The AGB sampling during 2021 started earlier than in 2020, hence an initial value close to 0 at the start of the 2021 season.

3.1 Aboveground Plant Biomass and Carbon Maps via UAV-LiDAR

The C-to-AGB ratios resulting from the lab analysis were $46.6 \pm 0.3\%$ for spring barley and $47.7 \pm 0.3\%$ for winter wheat. For simplicity, we assumed this ratio to be uniformly distributed along the AGB components (i.e. shoots, leaves, grain-bearing organs and grains). Therefore, the AGC and AGB prediction maps are linearly related (Figure 7).

Using the best performing regression model (i.e. ERT) resulted in a prediction performance of $\overline{R^2} : 0.72$, $\overline{RMSE} : 227$ g, $\overline{MAE} : 121$ g at a spatial resolution of 1 m^2 , on the validation sets, and the model was not overfitted. ERT outperformed the other two candidate models: XGBoost ($\overline{R^2} : 0.67$, $\overline{RMSE} : 250$ g, $\overline{MAE} : 182$ g) and Huber regressor ($\overline{R^2} : 0.70$, $\overline{RMSE} : 237$ g, $\overline{MAE} : 190$ g). Thus, based on performance evaluation on the validation sets, ERT was selected for AGB and AGC prediction. For further details in feature selection and specific information related to the processing pipeline, the reader is referred to Revenga et al. 2022 [30].

Via the spatially resolved regression outputs of the ERT model, we obtained surface-based maps of AGB and AGC. We visualized the AGB and AGC predictions based on the input UAV-LiDAR point cloud data, at 1 m^2 resolution in Figure 7. The values shown present a confidence interval of 68% of 108 gAGC/m^2 in barley, and 134 gAGC/m^2 in wheat, corresponding to 1 standard deviation over 10 random executions of the ERT prediction on the test sets (following the procedure described in Revenga et al., 2022) [30]. Then we selected nine UAV-LiDAR survey dates (five during 2020; four during 2021), and intersected them with the 70% of the area of influence surrounding the eddy-covariance station to visualize the spatially resolved model output.

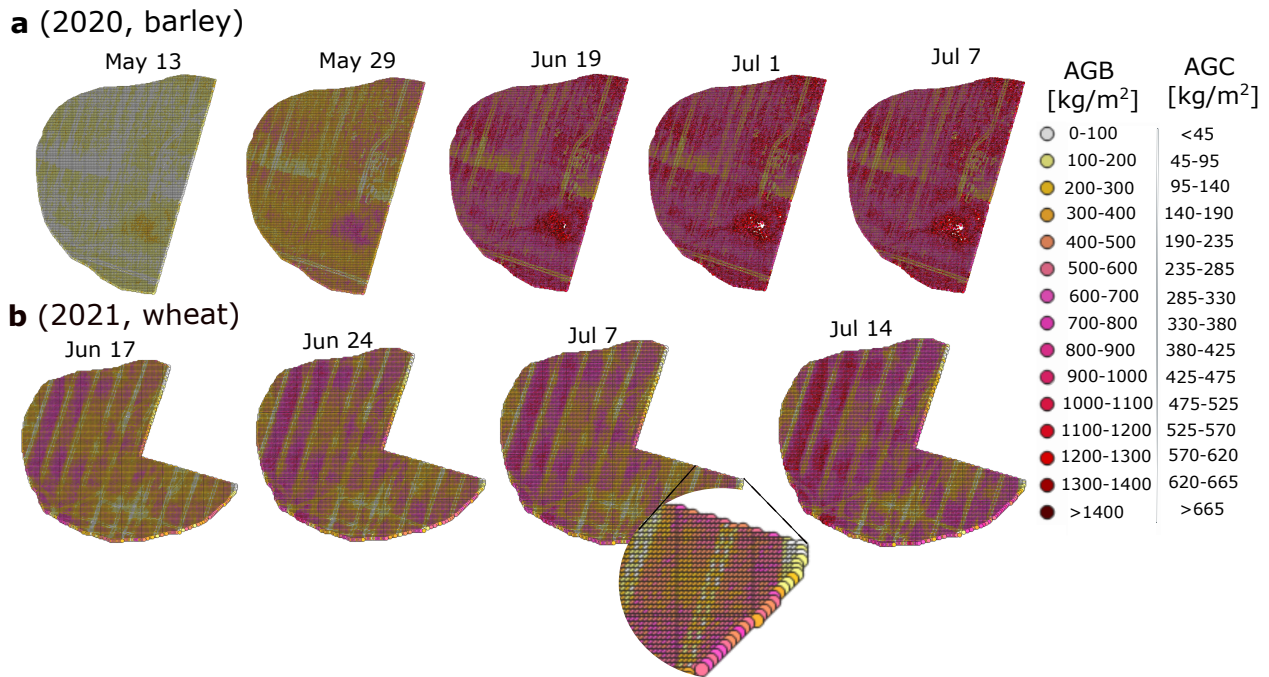


Figure 7. Exemplary aboveground biomass (AGB) and aboveground carbon (AGC) maps. **a:** 2020 growing season; **b:** 2021 growing season. Values in legend indicate predictions of dry AGB matter and the corresponding AGC value. A sector of the eddy covariance station footprint was clipped out to disregard the areas in wind directions affected by the instrumental plot: in 2020, the (18–198)^o wind directions were excluded; in 2021, the wind directions (18–116)^o were excluded. Both legends share the same color gradient since AGC is modeled as a linear function of AGB. The N-S stripping pattern is due to the field management (irrigation).

412

Above- and Belowground Carbon Estimates

413

414

415

416

417

418

419

420

Using the AGC assessment as reference, we modeled the belowground C component (i.e. root_C and C rhizodeposits), according to reference literature [64, 65], and phenology dependant allometry (Eq. 2). Figure 8 (a) shows the percentage of GPP translocated to above- and belowground components during the crops' lifecycle. Similarly, Figure 8 (b) shows the actual C stocks estimated (as a percentage of the total plant C), both in above- and belowground components. The values shown result from averaging the percentages reported in reference literature of isotope C pulse labeling, for the same crop type under similar soil and climatic conditions. They do not include C transfer to the soil as rhizodeposits.

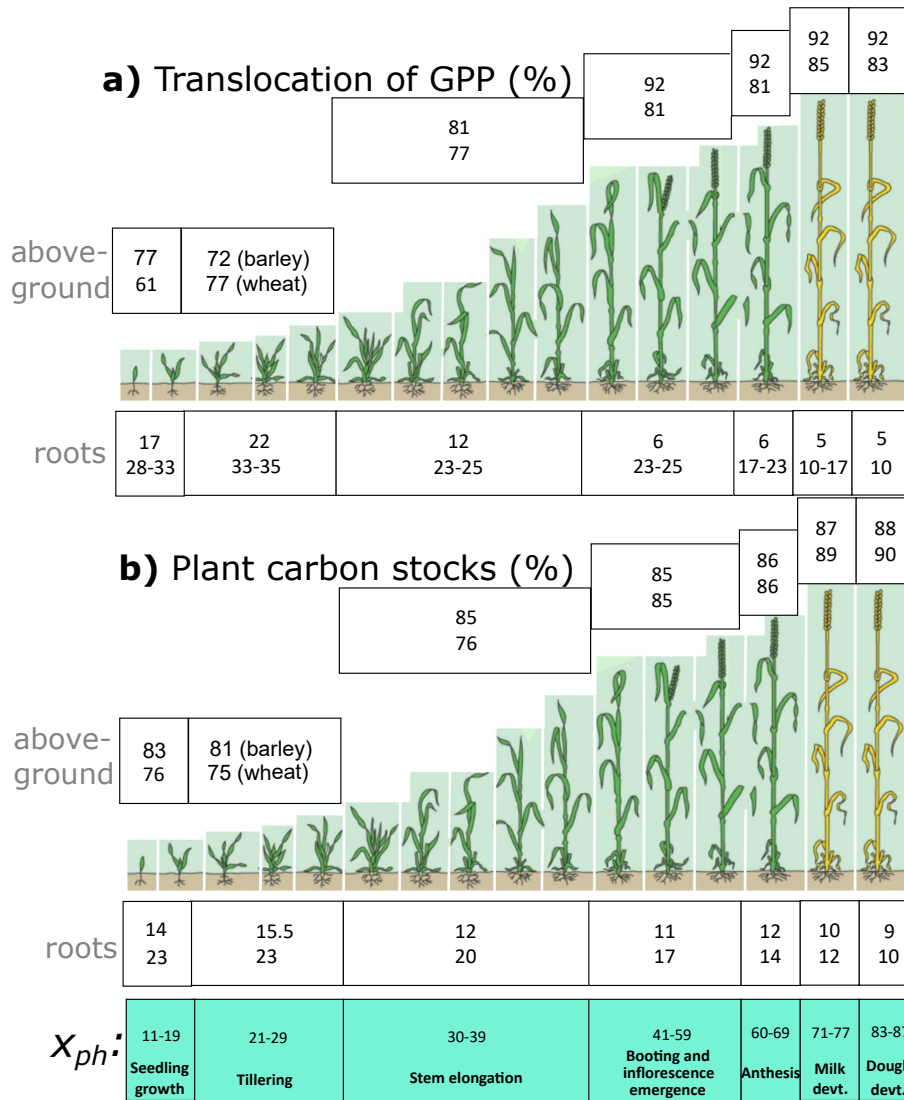


Figure 8. **a:** Translocation of photoassimilated atmospheric carbon (i.e. GPP) to aboveground and root components (without rhizodeposition); values in white boxes indicate estimated % corresponding to the same phenological growth stage. **b:** Plant carbon stocks along the growing season showing the estimated carbon allocation at each phenological stage. Percentage values of carbon in roots (both translocated and stocked) are derived from Kuzyakov et al. 2000 [65] for wheat and barley crops in sandy soils. Each white box shows values for spring barley (above) and winter wheat (below). x_{ph} : phenological growth stage (Zadoks decimal code) [67]. The inset indicating r.b.m. shows the stage when the root biomass maximum occurs. (Graphics adapted from Large et al., 1954) [74].

3.2 Comparing Flux Data and Plant Carbon Estimates from UAV-LiDAR

The cumulative NPP curves of the two growing seasons considered are shown in Figure 9. The trajectory of the NPP curve in the year 2020 exhibits an early start (by beginning of May), and reaches the saturation point by the last UAV-LiDAR survey (i.e. on July 22). In contrast, in 2021, NPP starts to grow visibly by ca. 20 May. Moreover, the last survey conducted in 2021 (i.e. July

426 14) coincides with a phase characterized by the ongoing upwards trajectory of the net ecosystem's
 427 uptake.

428 It can be observed a general agreement between the two methods, with a slight underestimation
 429 of the UAV-LiDAR assessment at the end of 2020, and a slight overestimation towards the end of
 430 the 2021 season.

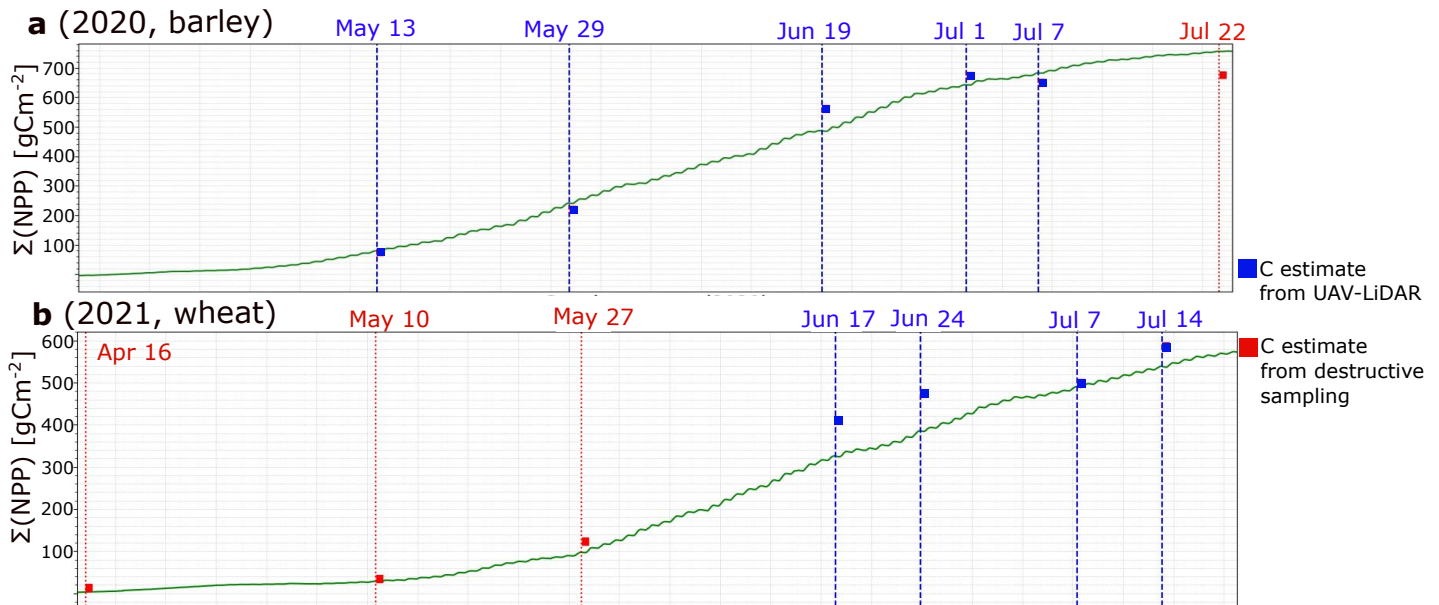


Figure 9. Cumulative NPP (gCm^{-2}) along (a) the 2020 and (b) the 2021 growing seasons (green curve). The red dotted vertical lines indicate aboveground biomass (AGB) sampling dates, while the blue dashed lines indicate dates in which both AGB sampling and UAV-LiDAR surveys took place. The square marks indicate the plant-C estimates for a given date using the UAV-LiDAR method (blue dates), or based on C estimated from destructive sampling (red dates).

431 We partitioned the different components of C uptake, in each of the two independent methods
 432 (whose compound values are shown Figure 9). This resulted in a per-component estimate of C
 433 stocks along the 2020 and 2021 growing seasons (Table 2). The results allow a comparison of the
 434 plant C estimates via the UAV-LiDAR method against the cumulative partitioned fluxes estimated
 435 via the eddy covariance method.

Table 2. Results of carbon estimates via the two fully independent methods considered. The first column indicates the UAV-LiDAR survey dates; second and third columns show the plant carbon stock estimated via the UAV-LiDAR method (both AGC and $root_C$); the last three columns show the cumulative values (from the start of the photosynthetic season) of the ecosystem flux components partitioned into net ecosystem exchange (NEE), heterotrophic respiration R_h and net primary productivity (NPP). x_{ph} indicates the average phenological growth stage (Zadoks decimal code) [67] measured at 12 control plots. $rhizo_C$: rhizodeposits.

Method		UAV-LiDAR			eddy covariance			
d/m/yyyy	x_{ph}	AGC [gm^{-2}]	$root_C$ [gm^{-2}]	$rhizo_C$	-NEE [gCm^{-2}]	R_h [gCm^{-2}]	NPP [gCm^{-2}]	
barley	13/5/2020	23	52.4	8.9	1.72	35.7	143.4	91.0
	29/5/2020	32	168.8	32.0	5.63	81.9	237.9	252.5
	19/6/2020	65	469.3	65.2	15.0	286.1	423.0	497.7
	1/7/2020	73	567.5	75.1	18.0	401.4	533.1	653.8
	7/7/2020	77	553.6	66.4	17.4	423.6	577.7	693.7
	22/7/2020	87	587.3	58.7	18.1	463.4	681.8	767.6
	16/4/2021	17	2.3	0.7	0.0	83.6	90.7	0.9
10/5/2021	31	18.4	5.5	0.3	147.6	100.8	25.5	
wheat	27/5/2021	37	86.7	25.8	1.1	68.6	229.5	94.5
	17/6/2021	47	341.9	55.5	4.0	102.5	418.4	321.3
	24/6/2021	57	402.7	58.0	4.7	144.3	482.0	372.5
	07/7/2021	71	434.1	50	4.9	227.3	592.1	486.1
	14/7/2021	77	522.6	48.5	5.8	251.5	672.1	532.0

436 The results of the date-by-date comparison of C estimates between the two methods are
 437 visualized in Figure 10. In each of the two tables (2020 shown above; 2021 shown below), the
 438 vertical axis indicates the survey date taken as reference for comparing a variation in C (Δ_C),
 439 while the horizontal axis shows the subsequent date considered for the comparison. In each cell of
 440 both tables, the values shown indicate the level of agreement between methods, in relative terms
 441 (i.e. %), where the reference value (i.e. 0%) is the flux-based method.

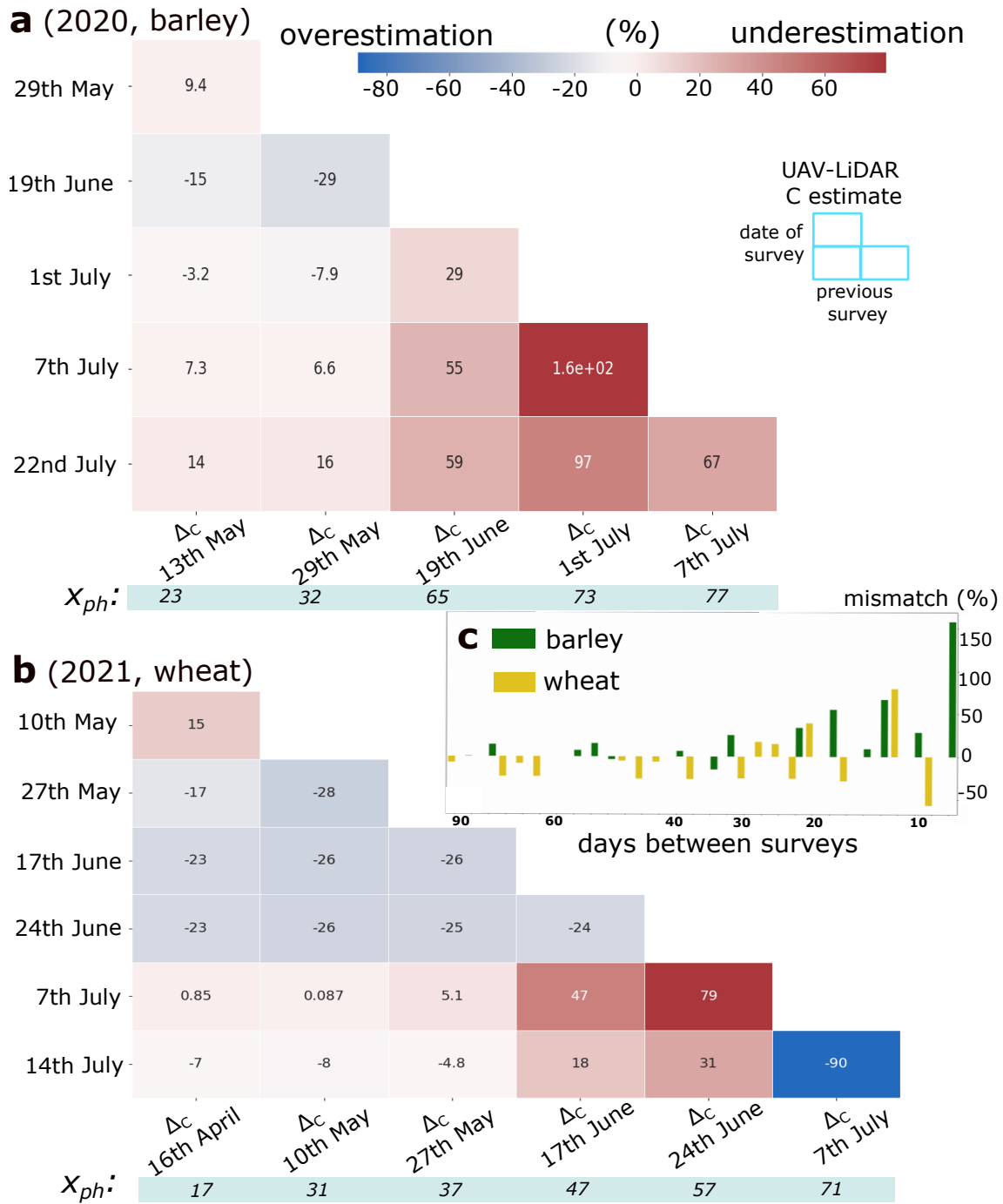


Figure 10. (Δ_C) values between pairs of surveying dates during the 2020 (a) and 2021 (b) growing seasons showing relative difference (%) between methods; the reference ($\Delta_C = 0\%$) is the cumulative NPP derived from the eddy covariance method at a given date. The inset (c) shows how the mismatch between methods is distributed, plotted against the time interval between survey dates (x-axis). It can be noted that (i) LiDAR estimates become more in agreement with NPP as time between surveys increases, and that (ii) considerable over- and underestimates are found between closely spaced dates during a late phenological stage (right tails of both a and b tables). x_{ph} indicates the average phenological growth stage.

4 = Discussion =

This study proposed a new method to acquire estimates of cumulative plant C stocks in cereal croplands using UAV-LiDAR and ML regression methods. The method presented was evaluated by comparing results against the cumulative NPP values measured via the eddy-covariance technique—i.e. the current state-of-the-art for ecosystem flux monitoring at the ecosystem scale. The match between the UAV-LiDAR estimates and the cumulative NPP, obtained via the eddy-covariance method, indicate that the crop C dynamics can be captured accurately with reliance on minimal mobile instrumentation. This finding is specially apparent when the first UAV-LiDAR survey date is taken early in the growing season. Conversely, comparisons lose consistency when time intervals between surveying dates are short, concurrently with a late phenological stage.

4.1 Plant Carbon Components from UAV-LiDAR: Values and Uncertainty

The values of AGC obtained via the spatially resolved predictions of the ERT model, taking UAV-LiDAR data as input were satisfactory at 1 m², and optimal at the flux footprint scale, due to spatial averaging effects [30, 61]. AGC was assumed linear with respect to AGB, following a constant ratio of $46.6 \pm 0.3\%$ of C-to-AGB in barley and $47.7 \pm 0.3\%$ in wheat, obtained via laboratory analysis. Therefore, the uncertainty estimate of the AGC component was assumed to be virtually the same as for AGB. While certain reference studies report of uneven C-to-AGB ratios across the plant components—e.g. leaves, root, grain bearing organs— [75], for simplicity, we assumed this ratio to stay constant across the plant components. Furthermore, the uncertainty on the lab analysis' results (i.e. $\pm 1\%$ of C-to-AGB ratio) is comparatively negligible with respect to the uncertainty derived from the provision of ground-truth instances (i.e. the noise contained in the AGC labels) [76, 77]. Such AGC label noise is an unavoidable source of error, as it represents the uncertainty of the provided reference values of AGC. We characterised it as the standard deviation of its distribution, and quantified it as 27.6% in barley, and 34.0% in wheat (details regarding this quantification of error are given in the Appendix of Revenga et al. 2022) [30].

With respect to the belowground components of the estimated C stocks, some observations must be made. Management practices and environmental factors can affect the root:shoot allometric ratio in cereal crops [64], and consequently alter this transfer of C into the ground [78, 79]. Therefore, however small in net values, such belowground biomass (BGB) estimates can be prone to bias or result largely uncertain [64]. Moreover, $root_C$ is much depending on soil water content, nutrient availability [80], as well as the phenological growth stage (as visualized in Figure 8). In fact, there is high variability in $root_C$ along the growing season, increasing steadily towards the flowering period (i.e. anthesis), and then gradually decreasing towards maturity [65], as nutrients are remobilized towards the developing seeds during the last developmental stages, sourcing from the senescing components (e.g. roots) [81, 82]. Here, in order to address this caveat, following the review by Hu et al. (2018) [64], we estimated the BGB at anthesis (which corresponds to the root biomass maximum in Figure 8), as given by the ratio $\frac{root_C}{(AGC+root_C)} = 0.10 \pm 0.01$. This ratio relates AGC at maturity and $root_C$ at anthesis, standardized to 25 cm soil depth. This ratio holds for conventional farming systems and is also supported by independent studies [83]. For barley, the absolute root biomass modeled at anthesis aligned tightly with empirical studies on root biomass [78]. The phenological growth stage [67] indicating anthesis was observed on 18 June 2020. Similarly, in 2021, the anthesis stage was estimated to correspond to 1 July 2021. Following this ratio, and the rate of photoassimilated C translocated to roots for barley and wheat in

485 sandy soils [65], we estimated the $root_C$ component at each biomass sampling date. At all events,
 486 we assumed that the ratios reported in reference literature [64] are robust and applicable to the
 487 environmental conditions and management type of the crops investigated in our study.

488 It is important to be aware of the potential sources of inconsistency between methods in order
 489 to avoid them. Crucially, in the context of collecting reference field data samples (i.e. ground
 490 truth), there is a possibility of unintentionally introducing a sample selection bias [76, 77]. Ideally,
 491 for the purpose of intercomparing cumulative C stocks, the locations selected for AGC sampling
 492 should be entirely randomized at every date across an area that is both (i) large enough, and (ii)
 493 either within the flux tower footprint or representative of the vegetation traits within the footprint.
 494 Here, a fully randomized sampling was the standard scheme for AGC data collection. However, it
 495 was deemed convenient to sample data differently on certain dates (e.g. 7 July of both 2020 and
 496 2021). On these campaigns, the sampling design was planned to enhance predictability of AGC
 497 using LiDAR-derived PCD data by collecting data from locations with contrasting AGB values.
 498 This approach allowed us to better capture the two-dimensional variability of AGC corresponding
 499 to the observed variations in the point cloud data scene. However, this resulted in an increased
 500 disagreement between the two independent methods to obtain carbon estimates when those dates
 501 were considered (see 7 of July in Figure 10, both in a and b). This outcome is statistically
 502 reasonable, as the continuous flux-based carbon estimates are independent and therefore unaffected
 503 by the AGC sampling design.

504 4.2 Ecosystem Carbon Uptake Derived from Flux Data

505 With respect to the estimated NPP, some observations should be made in the light of the
 506 presented results. Here, we modeled R_{soil} as a function of soil temperature, taking as sample data
 507 to model it the dates prior to the onset of the photosynthetic season (i.e. December–February).
 508 However, during these dates, air and soil temperatures did not span a wide range, staying close
 509 to frozen conditions. Therefore, the low dynamics in the values of soil temperature during the
 510 beginning of the year may have led to underestimations in the modeled R_{soil} . Accurately modeling
 511 heterotrophic soil respiration as a function of temperature may be challenging, particularly when
 512 the range of temperatures before shoot emergence (i.e. onset of photosynthetic season) is narrow.
 513 This can lead to added uncertainties in the predicted values of R_{soil} . In order to narrow this
 514 uncertainty source down, further studies should consider combining the setup we employed with soil
 515 gas flux measurements. Additionally, the exact dates of fertilizer deposition by the land managers
 516 remain unknown. The effect of such field management (e.g. fertilizer application, irrigation) cannot
 517 be reflected in the LiDAR derived C estimates, but do have an impact on the measured fluxes, e.g.
 518 enhancing R_{soil} upon application of organic fertilizers.

519 4.3 Comparing Flux Data and Plant Carbon Estimates from UAV-LiDAR

520 Figure 10 shows the result of the comparison of C stocks obtained via the two independent
 521 methods, i.e. the UAV-LiDAR method and the flux-based method. The results indicate show
 522 convergence between the two independently obtained estimates, and are shown as delta values
 523 (Δ_C , Eq. 3). Several observations can be made from these results:

- 524 • (i) The optimal reference date for comparing the increase in plant C stocks is the first day
 525 of the growing season, and this observation holds true for both years. When considering the

526 1st date as the reference, the mean error of predictions is the lowest obtained. In 2020, it is
 527 $2.5 \pm 10.4\%$, and in 2021, it is $-9.0 \pm 13.3\%$. These consistent results across both seasons
 528 indicate that this experimental setup is the best-performing one. When using the 2nd date
 529 as the reference, the mean error between independent estimates in 2020 is $-3 \pm 16.9\%$, and
 530 similarly, in 2021, it is $-8.9 \pm 11.4\%$. If we take the 3rd date as the reference for comparison,
 531 the findings in 2020 indicate a persistent underestimation of $47.6 \pm 13.3\%$. In contrast, the
 532 results for 2021 exhibit a closer approximation to the reference NPP value, with a deviation
 533 of $-12.7 \pm 13.3\%$.

- 534
- 535 • (ii) The right tail ends of both tables, denoting UAV-LiDAR surveys during the late season,
 536 reveal that comparing increments in C between closely spaced dates at a late phenological
 537 stage leads to noticeable over- and underestimates. Therefore, besides the temporal proxim-
 538 ity of survey dates, the phenological stage of the crops appears to exert a significant influence
 539 in the cumulative C stock predictions.
 - 540
 - 541 • (iii) In Figure 10, the inset panel (c) illustrates the Δ_C values of both crops over the tem-
 542 poral interval between survey dates (in x-axis). A clear trend can be observed, revealing a
 543 consistent increase in errors as the UAV-LiDAR survey dates become closer. This observed
 544 pattern in both growing seasons suggests that, irrespective of the crop type, estimates from
 545 surveys conducted in close temporal proximity tend to be suboptimal.

546 The observed disparities between the two methods considered fall within the uncertainty
 547 reported in reference studies between modeled and empirical approaches to estimate C stocks in
 548 croplands. For instance, a 18% of discrepancy between modeled and observed crop mass is reported
 549 by Soltani et al. (2012) [84]. However, we consider that the most noteworthy aspect of the proposed
 550 method is its ability to provide flexible estimates of CO₂ fluxes that align well with the EC flux
 551 estimates, and require minimal mobile instrumentation. Since the UAV-LiDAR estimates can be
 552 obtained without reliance on ground-based equipment, they enable assessments of CO₂ fluxes in
 553 agroecosystems that are hardly accessible and therefore remain to date poorly documented.

554 **5 = Conclusions =**

555 In this study, we developed and evaluated a method to estimate plant C stocks in managed
 556 cereal croplands, using UAV-LiDAR and machine learning (ML) regression methods. We bench-
 557 marked the results obtained by comparison with the corresponding cumulative NPP during the
 558 exact time period. From the obtained results, we conclude that total plant-mediated C stocks
 559 can be accurately estimated using UAV-LiDAR in combination with ML regression methods at
 560 the ecosystem scale. These estimates correspond to cumulative atmospheric CO₂ fluxes uptaken
 561 during the crop development. The match between the temporal development in CO₂ uptake within
 562 the footprint of the eddy covariance station, using the UAV-LiDAR based method, and the eddy
 563 covariance estimates showed an optimal mean error of $2.5 \pm 10.4\%$ in spring barley. In winter
 564 wheat, the optimal mean error was $-9.0 \pm 13.3\%$. These findings indicate that the comparisons
 565 of C stocks over the entire growing season, considering the first survey as the reference date, were
 566 the most accurate.

567 However, the results also show that it is crucial to consider that UAV-LiDAR estimates of
 568 CO₂ uptake may exhibit over- or underestimation under certain conditions, which should not pass

569 overlooked by further research studies and practitioners. This can occur when (i) LiDAR surveys
 570 are too close to one another, particularly during the later stages of phenological development, and
 571 (ii) a sample selection bias is introduced—during reference field data sampling. Therefore, care
 572 must be taken as regards allowing suitable time intervals between surveys and appropriate AGC
 573 sampling schemes. When comparing the resulting plant C values with eddy covariance estimates,
 574 a satisfactory level of agreement is observed, provided that the effects of AGC sampling design and
 575 time interval between UAV-LiDAR survey dates are taken into account.

576 We consider these results a promising step towards the data-driven upscaling of directly mea-
 577 sured fluxes during the growing season in managed ecosystems, as well as towards the interpolation
 578 of CO₂ fluxes across eddy covariance stations by leveraging mobile platforms, LiDAR technology
 579 and ML regression methods.

580 **6 = Author contributions =**

581 Original conceptual framework: TF, KT, JCR; methodology: JCR; experimental design: KT,
 582 TF, JCR; UAV-LiDAR data collection: JCR, KT; field-based data collection and curation: RJ,
 583 JCR, KT; laser data processing: JCR, KT; eddy covariance data collection and processing: RJ, TF,
 584 JCR; feature engineering, machine learning models' training and evaluation: JCR; visualisation:
 585 JCR and PR; project supervision: TF, KT; project administration: TF, KT; writing—original
 586 draft preparation: JCR; writing—review and editing: JCR, PR, TF, KT.

587 All contributing authors have read and agreed to the published version of the manuscript.

588 **7 = Acknowledgements =**

589 The authors acknowledge the contributions of René Lee, Lars Rasmussen, Rune Skov Mai-
 590 goord, Binsheng Gao, and Alek Wieckowski, in supporting the tasks of field data acquisition,
 591 contributing to this study as fieldwork and laboratory assistants.

592 **8 = Funding =**

593 This project has received funding support from the Talent Program Horizon 2020/Marie
 594 Skłodowska-Curie Actions, a Villum Experiment grant by the Velux Foundations, DK (MapCland
 595 project, project number: 00028314), the DeepCrop project (UCPH Strategic plan 2023 Data +
 596 Pool), as well as a UAS- ability infrastructure grant from Danish Agency for Science, Technology
 597 and Innovation. The authors acknowledge as well financial support from ICOS.

598 **9 List of abbreviations**

- 599 • AGB: aboveground biomass.
- 600 • AGC: aboveground carbon.
- 601 • EC: eddy covariance.
- 602 • ECB: ecosystem carbon balance.
- 603 • ERT: extreme randomized trees.
- 604 • GHG: greenhouse gas.
- 605 • GPP: gross primary productivity.

- 606 • ICOS: integrated carbon observation system.
- 607 • LiDAR: light detection and ranging.
- 608 • ML: machine learning.
- 609 • NECB: net ecosystem carbon balance.
- 610 • NEE: net ecosystem exchange.
- 611 • NPP: net primary productivity.
- 612 • PCD: point cloud data.
- 613 • R_a : autotrophic plant respiration.
- 614 • R_{eco} : ecosystem respiration.
- 615 • RF: random forest.
- 616 • R_h : heterotrophic respiration.
- 617 • $root_C$: carbon content in roots.
- 618 • Rsoil: microbial soil respiration.
- 619 • RS: remote sensing.
- 620 • $Rhizo_C$: carbon transferred to soil via rhizodeposition.
- 621 • UAV: unstaffed aerial vehicle.
- 622 • WDI: water deficit index.
- 623 • X_{ph} : crops growth stage (according to Zadoks decimal code).

624 **10 Annex I: NEE, NPP, GPP, R_{eco} in both growing seasons (2020 and 2021)**

625 Figure 11 displays the processed NEE over time for both years, with a 30-minute pixel reso-
 626 lution. It can be noted that in the 2020 season, there was an advancement of approximately 15
 627 days, and more concentrated C uptake hotspots between 11:00 and 14:00 in late June and late
 628 July compared to the 2021 season.

629 Remarkably, in Figure 12, it can be observed that the time series of cumulative NPP and R_{eco}
 630 never cross each other in 2021 (b), while they do so in 2020 (a). The enclosed area under these
 631 two curves indicates the rate of C accumulation efficiency with respect to ecosystem respiratory
 632 losses. It makes sense that in a more homogeneous, densely populated crop, the C uptake was
 633 more efficient than in the sparse crops of 2021.

634 These observations are consistent with the AGC sampling campaigns—where more sparse
 635 crops were sampled in the second year—and with the PCD representation of the cropfields (Figure
 636 3)—where a higher PCD porosity was found in the second year as well as a lower cumulative NPP
 637 flux (Figure 9).

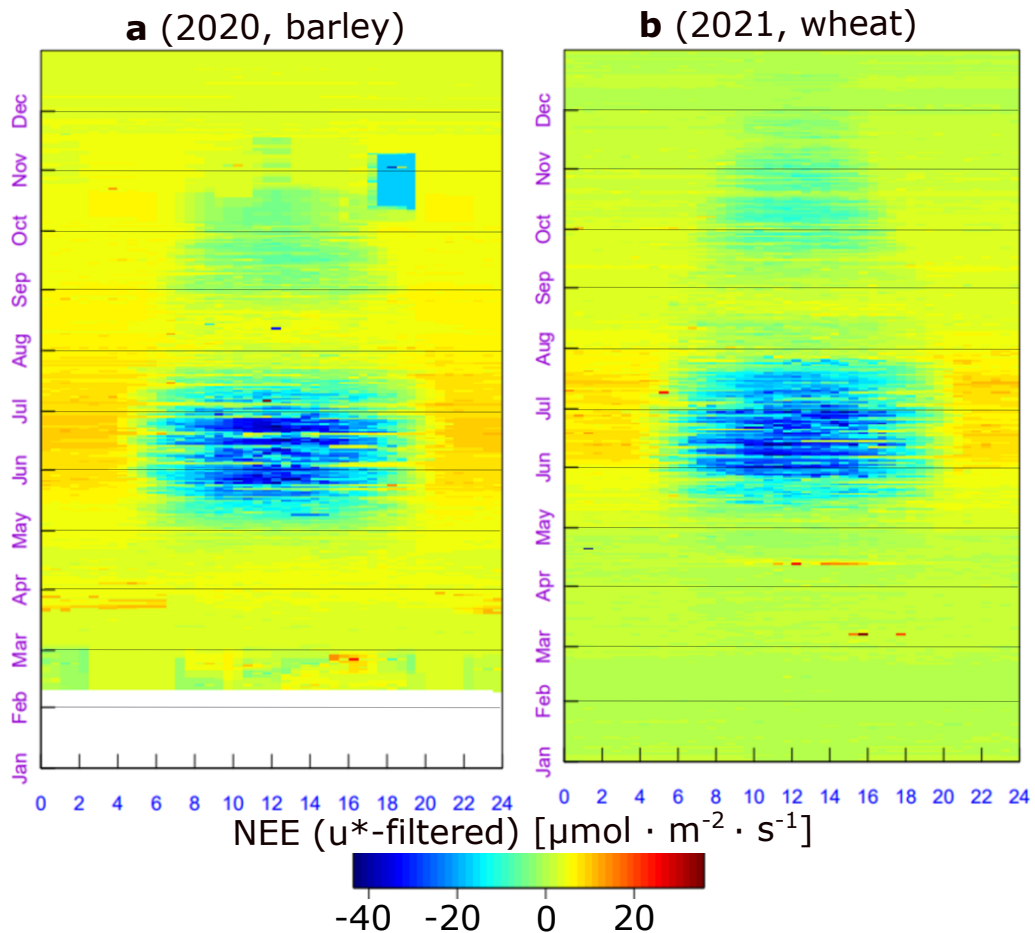


Figure 11. Measured net ecosystem exchange (NEE) at Voulundgaard research station during 2020 (a) and 2021 (b). Data displayed were gap-filled, spikes removed and u^* -filtered. It can be noted a delay in the onset of the growing season in 2021 with respect to 2020 of almost 3 weeks, including a false start in mid May, partly explained by the cold spell of 10-12th February (figure obtained from the REddyProcWeb online tool : www.bgc-jena.mpg.de/bgi/index.php/Services/REddyProcWeb).

638

References

639

- [1] David Laborde et al. “Agricultural subsidies and global greenhouse gas emissions”. In: *Nature communications* 12.1 (2021), p. 2601.
- [2] John R Porter, Mark Howden, and Pete Smith. “Considering agriculture in IPCC assessments”. In: *Nature Climate Change* 7.10 (2017), pp. 680–683.
- [3] Philip Thornton et al. “Agriculture in a changing climate: Keeping our cool in the face of the hothouse”. In: *Outlook on Agriculture* 47.4 (2018), pp. 283–290.
- [4] P. R. Shukla et al. *Summary for policymakers, in Climate Change Land: An IPCC Special Report on Climate Change Desertification, Land Degradation, Sustainable Land Management, Food Security, Greenhouse Gas Fluxes in Terrestrial Ecosystems*. Tech. rep. Intergovernmental Panel on Climate Change, 2023.

649

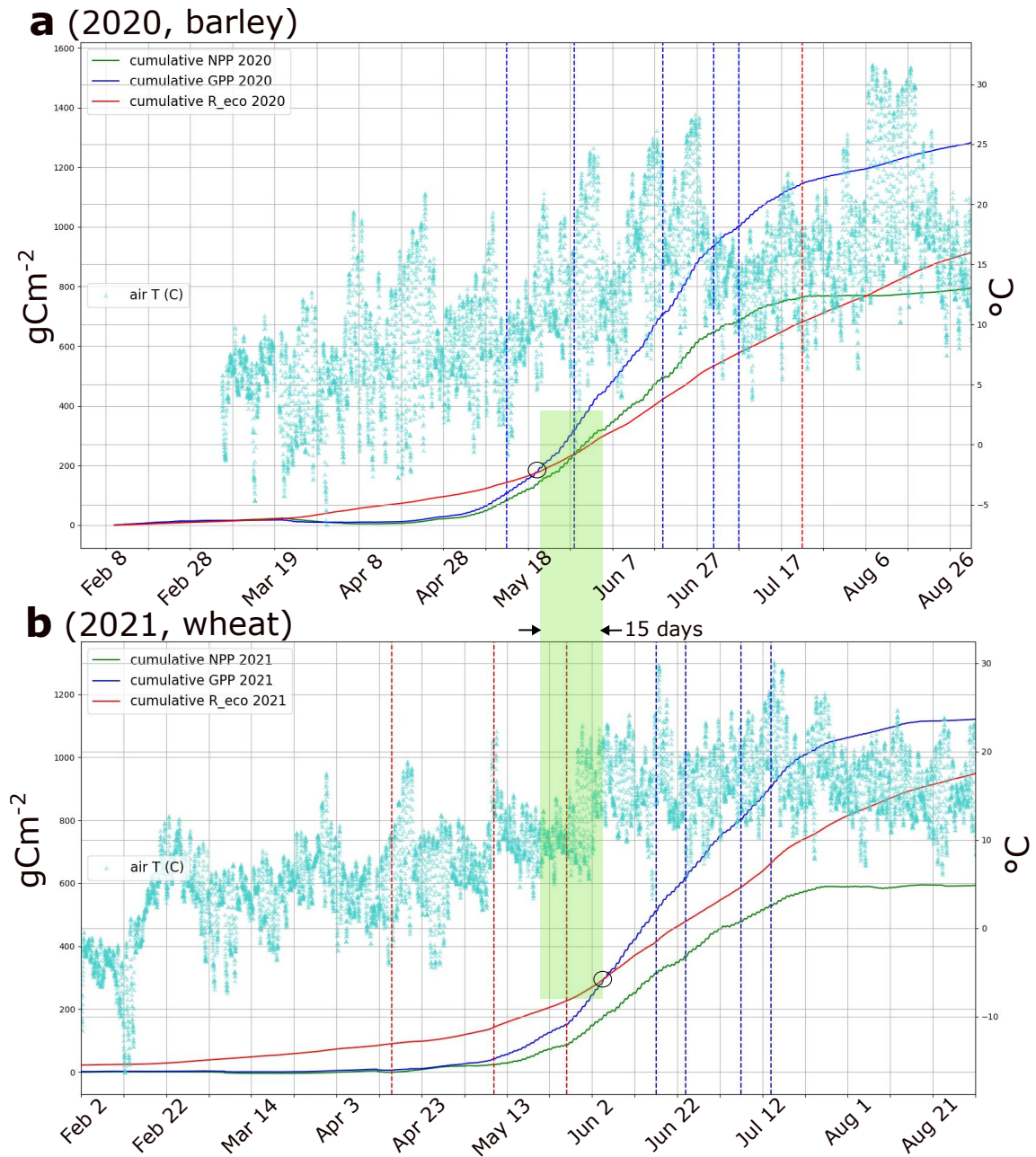


Figure 12. Estimated cumulative fluxes along the growing season of 2020 (a), and 2021 (b). GPP: gross primary productivity; R_{eco} : ecosystem respiration; NPP: net primary productivity. The red vertical lines indicate aboveground biomass (AGB) sampling dates, while the blue lines indicate dates in which both AGB sampling and UAV-LiDAR surveys took place. In both years, the black circles indicate the dates when GPP offsets R_{eco} . It can be observed how in 2021 this occurs on the 5th June, while in 2020 GPP reaches ecosystem respiratory losses on the 19th May, i.e. 16 days earlier. This delay in GPP during 2021 is partly explained due to the cold spell of February, damaging the early seedlings. The lack of temperatures at the beginning of 2020 (a) is due to a failure in the instrumental setup.

650

[5] Marco Springmann et al. "Options for keeping the food system within environmental limits".

651

In: *Nature* 562.7728 (2018), pp. 519–525.

- 652 [6] Gerald C Nelson et al. “Climate change effects on agriculture: Economic responses to
653 biophysical shocks”. In: *Proceedings of the National Academy of Sciences* 111.9 (2014),
654 pp. 3274–3279.
- 655 [7] Mitchell C Hunter et al. “Agriculture in 2050: recalibrating targets for sustainable intensi-
656 fication”. In: *Bioscience* 67.4 (2017), pp. 386–391.
- 657 [8] Hamid El Bilali et al. “Food and nutrition security and sustainability transitions in food
658 systems”. In: *Food and energy security* 8.2 (2019), e00154.
- 659 [9] Jonathan A Foley et al. “Solutions for a cultivated planet”. In: *Nature* 478.7369 (2011),
660 pp. 337–342.
- 661 [10] Tara Garnett et al. “Sustainable intensification in agriculture: premises and policies”. In:
662 *Science* 341.6141 (2013), pp. 33–34.
- 663 [11] David J Mulla. “Twenty five years of remote sensing in precision agriculture: Key advances
664 and remaining knowledge gaps”. In: *Biosystems engineering* 114.4 (2013), pp. 358–371.
- 665 [12] F Stuart Chapin, PA Matson, and PM Vitousek. *Principles of terrestrial ecosystem ecology*.
666 *Principles of Terrestrial Ecosystem Ecology*. 2012.
- 667 [13] YM Zhang et al. “Vegetation carbon sequestration in the Loess Plateau under the syner-
668 gistic effects of land cover change and elevations”. In: *Acta Ecologica Sinica* 42.10 (2022),
669 pp. 3897–3908.
- 670 [14] Peter M Anthoni et al. “Winter wheat carbon exchange in Thuringia, Germany”. In: *Agri-
671 cultural and Forest Meteorology* 121.1-2 (2004), pp. 55–67.
- 672 [15] Ulises Mariano Marconato, Roberto J Fernández, and Gabriela Posse Beaulieu. *Cropland
673 Net Ecosystem Exchange Estimation for the Inland Pampas (Argentina) Using EVI, Land
674 Cover Maps, and Eddy Covariance Fluxes*. Tech. rep. Frontiers Media, 2022.
- 675 [16] Arne Poyda et al. “Carbon fluxes and budgets of intensive crop rotations in two regional
676 climates of southwest Germany”. In: *Agriculture, Ecosystems & Environment* 276 (2019),
677 pp. 31–46.
- 678 [17] Anne-Katrin Prescher, Thomas Grünwald, and Christian Bernhofer. “Land use regulates
679 carbon budgets in eastern Germany: From NEE to NBP”. In: *Agricultural and Forest Me-
680 teorology* 150.7-8 (2010), pp. 1016–1025.
- 681 [18] Rasmus Jensen, Mathias Herbst, and Thomas Friberg. *Direct and indirect controls of the
682 interannual variability in atmospheric CO₂ exchange of three contrasting ecosystems in
683 Denmark*. 2016.
- 684 [19] Praveena Krishnan et al. “Factors controlling the interannual variability in the carbon
685 balance of a southern boreal black spruce forest”. In: *Journal of Geophysical Research:
686 Atmospheres* 113.D9 (2008).
- 687 [20] Christopher B Field and Jörg Kaduk. “The carbon balance of an old-growth forest: building
688 across approaches”. In: *Ecosystems* 7 (2004), pp. 525–533.
- 689 [21] Mark E Harmon et al. “Production, respiration, and overall carbon balance in an old-growth
690 Pseudotsuga-Tsuga forest ecosystem”. In: *Ecosystems* 7 (2004), pp. 498–512.
- 691 [22] Heather Keith, Brendan G Mackey, and David B Lindenmayer. “Re-evaluation of forest
692 biomass carbon stocks and lessons from the world’s most carbon-dense forests”. In: *Pro-
693 ceedings of the National Academy of Sciences* 106.28 (2009), pp. 11635–11640.
- 694 [23] Scott D Miller et al. “Biometric and micrometeorological measurements of tropical forest
695 carbon balance”. In: *Ecological Applications* 14.sp4 (2004), pp. 114–126.

- 696 [24] Jian Wu et al. “Synthesis on the carbon budget and cycling in a Danish, temperate deciduous
697 forest”. In: *Agricultural and Forest Meteorology* 181 (2013), pp. 94–107.
- 698 [25] Thomas Foken, Marc Aubinet, and Ray Leuning. “The eddy covariance method”. In: *Eddy
699 covariance: a practical guide to measurement and data analysis*. Springer, 2011, pp. 1–19.
- 700 [26] Sheng Wang et al. “Temporal interpolation of land surface fluxes derived from remote
701 sensing—results with an unmanned aerial system”. In: *Hydrology and Earth System Sciences*
702 24.7 (2020), pp. 3643–3661.
- 703 [27] Helene Hoffmann et al. “Crop water stress maps for an entire growing season from visible
704 and thermal UAV imagery”. In: *Biogeosciences* 13.24 (2016), pp. 6545–6563.
- 705 [28] Derek Hollenbeck and YangQuan Chen. “Multi-UAV method for continuous source rate
706 estimation of fugitive gas emissions from a point source”. In: *2021 International Conference
707 on Unmanned Aircraft Systems (ICUAS)*. IEEE, 2021, pp. 1308–1313.
- 708 [29] Derek Hollenbeck et al. “Evaluating a UAV-based mobile sensing system designed to quan-
709 tify ecosystem-based methane”. In: *Authorea Preprints* (2022).
- 710 [30] Jaime C Revenga et al. “Above-Ground Biomass Prediction for Croplands at a Sub-Meter
711 Resolution Using UAV–LiDAR and Machine Learning Methods”. In: *Remote Sensing* 14.16
712 (2022), p. 3912.
- 713 [31] N Ace Pugh et al. “Temporal estimates of crop growth in sorghum and maize breeding
714 enabled by unmanned aerial systems”. In: *The Plant Phenome Journal* 1.1 (2018), pp. 1–
715 10.
- 716 [32] Wang Li et al. “Remote estimation of canopy height and aboveground biomass of maize
717 using high-resolution stereo images from a low-cost unmanned aerial vehicle system”. In:
718 *Ecological indicators* 67 (2016), pp. 637–648.
- 719 [33] Abdullah M Al-Sadi et al. “Genetic analysis reveals diversity and genetic relationship among
720 Trichoderma isolates from potting media, cultivated soil and uncultivated soil”. In: *BMC
721 microbiology* 15 (2015), pp. 1–11.
- 722 [34] Sebastian Varela et al. “Spatio-temporal evaluation of plant height in corn via unmanned
723 aerial systems”. In: *Journal of Applied Remote Sensing* 11.3 (2017), pp. 036013–036013.
- 724 [35] J Bendig et al. “Very high resolution crop surface models (CSMs) from UAV-based stereo
725 images for rice growth monitoring in Northeast China”. In: *Int. Arch. Photogramm. Remote
726 Sens. Spat. Inf. Sci* 40 (2013), pp. 45–50.
- 727 [36] Juliane Bendig et al. “Estimating biomass of barley using crop surface models (CSMs)
728 derived from UAV-based RGB imaging”. In: *Remote sensing* 6.11 (2014), pp. 10395–10412.
- 729 [37] Sebastian Brocks and Georg Bareth. “Estimating barley biomass with crop surface models
730 from oblique RGB imagery”. In: *Remote Sensing* 10.2 (2018), p. 268.
- 731 [38] Tianxing Chu et al. “Cotton growth modeling and assessment using unmanned aircraft sys-
732 tem visual-band imagery”. In: *Journal of Applied Remote Sensing* 10.3 (2016), pp. 036018–
733 036018.
- 734 [39] T Jensen et al. “Detecting the attributes of a wheat crop using digital imagery acquired
735 from a low-altitude platform”. In: *Computers and electronics in agriculture* 59.1-2 (2007),
736 pp. 66–77.
- 737 [40] E Raymond Hunt et al. “NIR-green-blue high-resolution digital images for assessment of
738 winter cover crop biomass”. In: *GIScience & remote sensing* 48.1 (2011), pp. 86–98.

- 739 [41] Maria Tattaris, Matthew P Reynolds, and Scott C Chapman. “A direct comparison of re-
740 mote sensing approaches for high-throughput phenotyping in plant breeding”. In: *Frontiers*
741 *in plant science* 7 (2016), p. 1131.
- 742 [42] Jakob Geipel et al. “A programmable aerial multispectral camera system for in-season crop
743 biomass and nitrogen content estimation”. In: *Agriculture* 6.1 (2016), p. 4.
- 744 [43] Jibo Yue et al. “Estimation of winter wheat above-ground biomass using unmanned aerial
745 vehicle-based snapshot hyperspectral sensor and crop height improved models”. In: *Remote*
746 *Sensing* 9.7 (2017), p. 708.
- 747 [44] Roope Näsi et al. “Estimating biomass and nitrogen amount of barley and grass using UAV
748 and aircraft based spectral and photogrammetric 3D features”. In: *Remote Sensing* 10.7
749 (2018), p. 1082.
- 750 [45] Angela Kross et al. “Assessment of RapidEye vegetation indices for estimation of leaf area
751 index and biomass in corn and soybean crops”. In: *International Journal of Applied Earth*
752 *Observation and Geoinformation* 34 (2015), pp. 235–248.
- 753 [46] Kishore C Swain, Steven J Thomson, and Hemantha PW Jayasuriya. “Adoption of an
754 unmanned helicopter for low-altitude remote sensing to estimate yield and total biomass of
755 a rice crop”. In: *Transactions of the ASABE* 53.1 (2010), pp. 21–27.
- 756 [47] Jordan Steven Bates et al. “Estimating canopy density parameters time-series for winter
757 wheat using UAS Mounted LiDAR”. In: *Remote Sensing* 13.4 (2021), p. 710.
- 758 [48] ICOS. *Integrated Carbon Observation System*. 2023. URL: <https://www.icos-cp.eu/>
759 (visited on 02/04/2023).
- 760 [49] Danish Ministry of Environment. *Order on the use of fertilisers by agriculture for the*
761 *2020/2021 planning period*. 2021. URL: [https://www.retsinformation.dk/eli/lta/](https://www.retsinformation.dk/eli/lta/2020/1166)
762 [2020/1166](https://www.retsinformation.dk/eli/lta/2020/1166). (accessed: 25.10.2021).
- 763 [50] L Davidson et al. “Airborne to UAS LiDAR: An analysis of UAS LiDAR ground control
764 targets”. In: *ISPRS Geospatial Week 2019* (2019).
- 765 [51] Bert Gielen et al. “Ancillary vegetation measurements at ICOS ecosystem stations”. In:
766 *International Agrophysics* 32.4 (2018), pp. 645–664.
- 767 [52] Jouni Heiskanen et al. “The integrated carbon observation system in Europe”. In: *Bulletin*
768 *of the American Meteorological Society* 103.3 (2022), E855–E872.
- 769 [53] S Sabbatini and D Papale. *ICOS Ecosystem Instructions for Turbulent Flux Measurements*
770 *of CO₂, Energy and Momentum (Version 20180110)*, ICOS Ecosystem Thematic Centre.
771 2017.
- 772 [54] Dean Vickers and L Mahrt. “Quality control and flux sampling problems for tower and
773 aircraft data”. In: *Journal of atmospheric and oceanic technology* 14.3 (1997), pp. 512–526.
- 774 [55] E. K. Webb, G. I. Pearman, and R. Leuning. “Correction of flux measurements for den-
775 sity effects due to heat and water vapour transfer”. In: *Quarterly Journal of the Royal*
776 *Meteorological Society* 106.447 (1980), pp. 85–100.
- 777 [56] Claudia Liebethal and Thomas Foken. “On the significance of the Webb correction to
778 fluxes”. In: *Boundary-Layer Meteorology* 109 (2003), pp. 99–106.
- 779 [57] JB Moncrieff et al. “A system to measure surface fluxes of momentum, sensible heat, water
780 vapour and carbon dioxide”. In: *Journal of Hydrology* 188 (1997), pp. 589–611.
- 781 [58] Dario Papale et al. “Towards a standardized processing of Net Ecosystem Exchange mea-
782 sured with eddy covariance technique: algorithms and uncertainty estimation”. In: *Biogeo-*
783 *sciences* 3.4 (2006), pp. 571–583.

- 784 [59] Markus Reichstein et al. “On the separation of net ecosystem exchange into assimilation
785 and ecosystem respiration: review and improved algorithm”. In: *Global change biology* 11.9
786 (2005), pp. 1424–1439.
- 787 [60] Natascha Kljun, MW Rotach, and HP Schmid. “A three-dimensional backward Lagrangian
788 footprint model for a wide range of boundary-layer stratifications”. In: *Boundary-Layer
789 Meteorology* 103 (2002), pp. 205–226.
- 790 [61] Scott Goetz and Ralph Dubayah. “Advances in remote sensing technology and implications
791 for measuring and monitoring forest carbon stocks and change”. In: *Carbon Management
792* 2.3 (2011), pp. 231–244.
- 793 [62] Francis Stuart Chapin et al. “Principles of terrestrial ecosystem ecology”. In: (2002).
- 794 [63] John Lloyd and JA Taylor. “On the temperature dependence of soil respiration”. In: *Func-
795 tional ecology* (1994), pp. 315–323.
- 796 [64] Teng Hu et al. “Root biomass in cereals, catch crops and weeds can be reliably estimated
797 without considering aboveground biomass”. In: *Agriculture, Ecosystems & Environment* 251
798 (2018), pp. 141–148.
- 799 [65] Yakov Kuzyakov and Grzegorz Domanski. “Carbon input by plants into the soil. Review”.
800 In: *Journal of Plant Nutrition and Soil Science* 163.4 (2000), pp. 421–431.
- 801 [66] JA Palta and PJ Gregory. “Drought affects the fluxes of carbon to roots and soil in ¹³C
802 pulse-labelled plants of wheat”. In: *Soil Biology and Biochemistry* 29.9-10 (1997), pp. 1395–
803 1403.
- 804 [67] Jan C Zadoks, Ting T Chang, Cal F Konzak, et al. “A decimal code for the growth stages
805 of cereals.” In: *Weed research* 14.6 (1974), pp. 415–421.
- 806 [68] Erick Zagal, Sigfus Bjarnason, and ULF Olsson. “Carbon and nitrogen in the root-zone of
807 barley (*Hordeum vulgare* L.) supplied with nitrogen fertilizer at two rates”. In: *Plant and
808 Soil* 157 (1993), pp. 51–63.
- 809 [69] Peter J Huber. “Robust statistics”. In: *International encyclopedia of statistical science*.
810 Springer, 2011, pp. 1248–1251.
- 811 [70] Art B Owen. “A robust hybrid of lasso and ridge regression”. In: *Contemporary Mathematics*
812 443.7 (2007), pp. 59–72.
- 813 [71] Pierre Geurts, Damien Ernst, and Louis Wehenkel. “Extremely randomized trees”. In: *Ma-
814 chine learning* 63.1 (2006), pp. 3–42.
- 815 [72] Tianqi Chen et al. “Xgboost: extreme gradient boosting”. In: *R package version 0.4-2* 1.4
816 (2015), pp. 1–4.
- 817 [73] Leo Breiman. “Random forests”. In: *Machine learning* 45.1 (2001), pp. 5–32.
- 818 [74] Ernest C Large et al. “Growth stages in cereals. Illustration of the Feekes scale.” In: *Plant
819 pathology* 3 (1954), pp. 128–129.
- 820 [75] Iker Aranjuelo et al. “Carbon and nitrogen partitioning during the post-anthesis period is
821 conditioned by N fertilisation and sink strength in three cereals”. In: *Plant Biology* 15.1
822 (2013), pp. 135–143.
- 823 [76] Joaquin Quinonero-Candela et al. *Dataset shift in machine learning*. Mit Press, 2008.
- 824 [77] Shai Ben-David et al. “A theory of learning from different domains”. In: *Machine learning*
825 79 (2010), pp. 151–175.
- 826 [78] Liisa Pietola and Laura Alakukku. “Root growth dynamics and biomass input by Nordic
827 annual field crops”. In: *Agriculture, ecosystems & environment* 108.2 (2005), pp. 135–144.

- 828 [79] MA Bolinder, DA Angers, and JP Dubuc. “Estimating shoot to root ratios and annual
829 carbon inputs in soils for cereal crops”. In: *Agriculture, ecosystems & environment* 63.1
830 (1997), pp. 61–66.
- 831 [80] Judah D Grossman and Kevin J Rice. “Evolution of root plasticity responses to variation
832 in soil nutrient distribution and concentration”. In: *Evolutionary Applications* 5.8 (2012),
833 pp. 850–857.
- 834 [81] Assaf Distelfeld, Raz Avni, and Andreas M Fischer. “Senescence, nutrient remobilization,
835 and yield in wheat and barley”. In: *Journal of experimental botany* 65.14 (2014), pp. 3783–
836 3798.
- 837 [82] Per L Gregersen. “Senescence and nutrient remobilization in crop plants”. In: *The molecular
838 and physiological basis of nutrient use efficiency in crops* (2011), pp. 83–102.
- 839 [83] Ngonidzashe Chirinda, Jørgen E Olesen, and John R Porter. “Root carbon input in organic
840 and inorganic fertilizer-based systems”. In: *Plant and Soil* 359 (2012), pp. 321–333.
- 841 [84] Afshin Soltani. *Modeling physiology of crop development, growth and yield*. CABi, 2012.